



HAL
open science

Geochemistry of Eocene-Early Oligocene low-temperature crustal melts from Greater Himalayan Sequence (Nepal): a nanogranitoid perspective

Omar Bartoli, Antonio Acosta-Vigil, Bernardo Cesare, Laurent Remusat,
Adriana Gonzalez-Cano, Markus Wälle, Lucie Tajčmanová, Antonio Langone

► **To cite this version:**

Omar Bartoli, Antonio Acosta-Vigil, Bernardo Cesare, Laurent Remusat, Adriana Gonzalez-Cano, et al.. Geochemistry of Eocene-Early Oligocene low-temperature crustal melts from Greater Himalayan Sequence (Nepal): a nanogranitoid perspective. Contributions to Mineralogy and Petrology, 2019, 174 (10), 10.1007/s00410-019-1622-2 . hal-02959315

HAL Id: hal-02959315

<https://hal.science/hal-02959315>

Submitted on 24 Dec 2020

HAL is a multi-disciplinary open access archive for the deposit and dissemination of scientific research documents, whether they are published or not. The documents may come from teaching and research institutions in France or abroad, or from public or private research centers.

L'archive ouverte pluridisciplinaire **HAL**, est destinée au dépôt et à la diffusion de documents scientifiques de niveau recherche, publiés ou non, émanant des établissements d'enseignement et de recherche français ou étrangers, des laboratoires publics ou privés.

Geochemistry of Eocene-Early Oligocene low-temperature crustal melts from Greater Himalayan Sequence (Nepal): a nanogranitoid perspective

Omar Bartoli^{1*}, Antonio Acosta-Vigil², Bernardo Cesare¹, Laurent Remusat³, Adriana Gonzalez-Cano³, Markus Wälle⁴, Lucie Tajčmanová⁵, Antonio Langone⁶

¹ *Dipartimento di Geoscienze, Università degli Studi di Padova, Padova, Italy*

² *Instituto Andaluz de Ciencias de la Tierra, CSIC-Universidad de Granada, Spain*

³ *Muséum National d'Histoire Naturelle, Sorbonne Université, UMR CNRS 7590, IRD, Institut de Minéralogie, de Physique des Matériaux et de Cosmochimie, IMPMC, Paris, France*

⁴ *REAIT, CRC and CFI Services (CCCS), Memorial University of Newfoundland, Canada*

⁵ *Institute of Earth Sciences, Heidelberg University, Germany*

⁶ *Istituto di Geoscienze e Georisorse, C.N.R. University of Pavia, Pavia, Italy*

* corresponding author: omar.bartoli@unipd.it, +390498279832

Abstract

Despite melt inclusions in migmatites and granulites have provided a wealth of information on crustal anatexis in different geological scenarios, yet a complete compositional study (including trace elements and H₂O) is missing for the Himalayas. In this contribution, we focus on nanogranitoids occurring in peritectic garnet of migmatites from Kali Gandaki valley in central Nepal (Greater Himalayan Sequence, GHS). Their microstructural position proves that these melts were produced at 650–720 °C and 1.0–1.1 GPa, during the Eohimalayan prograde metamorphism (41–36 Ma) associated to crustal thickening. Nanogranitoid compositions (mostly granodiorites, tonalities and trondhjemites) resemble those of experimental melts produced during H₂O-present melting of metasedimentary rocks. They have variable H₂O concentrations (6.5–14.4 wt%), which approximate the expected minimum and maximum values for crustal melts produced at the inferred P–T conditions. These compositional signatures suggest that melt formation occurred in the proximity of the

1 H₂O-saturated solidus, in a rock-buffered system. The low to very low contents of Zr (3–8
2 ppm), Th (0.1–1.2 ppm) and LREE (4–11 ppm) along with the weak to moderate positive Eu
3 anomalies (Eu/Eu* =1.2–3.3), the high B concentrations (200–3400 ppm) and the high U/Th
4 ratio (up to 21) point to the lack of equilibration between melt and accessory minerals and are
5 consistent with melting of plagioclase at low temperature. Kali Gandaki nanogranitoids have
6 recorded the beginning of melting in a H₂O-present scenario that, in other GHS localities,
7 may have produced voluminous crustal melts. We demonstrate that compositional
8 comparison with nanogranitoids may be useful to reconstruct the petrogenesis of
9 Eohimalayan granitoids.
10
11
12
13
14
15
16
17
18
19
20
21
22
23

24 **Keywords:** Nanogranitoids, Greater Himalayan Sequence, low-T crustal melts, H₂O-present
25 melting
26
27
28
29
30
31
32
33
34
35
36
37
38
39
40
41
42
43
44
45
46
47
48
49
50
51
52
53
54
55
56
57
58
59
60
61
62
63
64
65

1 Introduction

2 The Himalaya mountain belt is the largest active collisional orogen on our planet and is an
3 ideal natural laboratory for investigating orogenic processes (Kohn 2014). This mountain
4 chain has resulted from collision between India and Asia at c. 59 Ma (Hu et al. 2016). The
5 structural and metamorphic evolution of this orogenic belt is divided into two main phases
6 (Hodges 2000): an Eocene-Late Oligocene Eohimalayan phase during which crustal
7 thickening occurred and most metamorphic rocks reached peak conditions in the kyanite
8 stability field, and an Early Miocene to present Neohimalayan phase characterized by
9 formation of sillimanite-bearing rocks and leucogranites which intruded the higher portions
10 of the Himalayan belt – the so called “Himalayan leucogranites” – whose largest plutons
11 formed at c. 21 Ma (Harrison 2006).

12 Himalayan leucogranites and the associated Miocene migmatites have been
13 investigated for decades (Weinberg 2016 and references therein). A number of works have
14 established that Miocene anatexis and leucogranite formation occurred by fluid-absent
15 melting of muscovite during decompression (e.g., Inger and Harris 1992; Pognante and
16 Benna 1993; Harris et al. 1995; Harris and Massey 1994; Davidson et al. 1997). Recently,
17 some works have argued that decompression was a consequence rather than a cause of
18 melting (e.g., Rubatto et al. 2013) and the recent review paper by Weinberg (2016) has
19 demonstrated the complexity of Neohimalayan anatexis which records differences in P–T–
20 X_{H_2O} conditions, timing and duration across the Himalayas.

21 Unlike for the Neohimalayan phase, much fewer constraints are available on anatexis
22 occurred during crustal thickening (i.e., the Eohimalayan anatexis), partly because of
23 pervasive Miocene thermal overprint. Where evidence exists, the majority of works have
24 dealt with the age and P–T conditions of high-grade metamorphic processes (e.g. Hodges et
25 al. 1996; Godin et al. 2001; Groppo et al. 2010; Zhang et al. 2010, 2015, 2017; Guilmette et

26 al. 2011; Rubatto et al. 2013; Palin et al. 2014; Wang et al. 2013; 2015; Iaccarino et al. 2017),
27 without shedding light on the composition of crustal melts which, in turn, may provide
28 important, and otherwise impossible to retrieve, information on melting mechanisms (e.g.,
29 Acosta-Vigil et al. 2010, 2012, 2017; Sawyer 2010, Carvalho et al. 2016, 2017, 2018;
30 Weinberg and Hasalová 2015a). For instance, an unusual Ca-rich leucogranite of Late
31 Oligocene age (c. 27.5 Ma) was considered to provide a rare insight into the pre-Miocene
32 melting associated to crustal thickening (Zhang et al. 2004).

33 In this contribution, we present for the first time the trace element and H₂O content of
34 melt inclusions (i.e., nanogranitoid inclusions or simply nanogranitoids; Cesare et al. 2015;
35 Bartoli et al. 2013a, 2016a; Ferrero and Angel 2018) from the Himalaya mountain belt.
36 Nanogranitoids come from the Greater Himalayan Sequence –which constitutes the high-
37 grade crystalline core of the orogen– and are present in a microstructural position that clearly
38 proves an Eohimalayan origin for these droplets of crustal melt (Carosi et al. 2015).

41 **Geological background and sampling**

42 From south to north, the Himalayan belt is divided into four tectonic units –Sub-
43 Himalayas molasses, Lesser Himalayan Sequence, Greater Himalayan Sequence (GHS) and
44 Tethyan Himalayan Sequence (THS)– which are separated by important tectonic structures,
45 i.e. Main Boundary Thrust, Main Central Thrust (MCT) and South Tibetan Detachment
46 System (Hodges 2000 and references therein; Fig. 1a). The GHS is a 20-30 km thick
47 sequence of medium- to high-grade metamorphic rocks and represents the metamorphic core
48 of the Himalaya (Searle and Godin 2003). Several levels of tectono-metamorphic
49 discontinuities were identified within the GHS (Carosi et al. 2018).

50 The sample under investigation comes from the N–S trending Kali Gandaki valley of
51 central Nepal (Fig. 1b), one of the most classic study areas of the Himalaya (see Carosi et al.

1
2
3
4
5
6
7
8
9
10
11
12
13
14
15
16
17
18
19
20
21
22
23
24
25
26
27
28
29
30
31
32
33
34
35
36
37
38
39
40
41
42
43
44
45
46
47
48
49
50
51
52 2014 and references therein). Here, GHS reaches a structural thickness of 10–15 km (Godin
53 2003), shows a NE-dipping prominent high-grade foliation with SW-verging isoclinal folds
54 (Brown and Nazarchuk 1993; Godin 2003; Kellett and Godin 2009; Searle 2010) and can be
55 subdivided in three units (Searle and Godin 2003; Searle 2010): the lowest Unit 1 is
56 represented by kyanite-bearing gneisses and migmatites, the Unit 2 consists of
57 clinopyroxene-garnet-amphibole-bearing calcsilicate gneisses, whereas Unit 3 is made of
58 orthogneisses and minor metapelites.

59 The nanogranitoid-bearing garnet crystal selected for this study has been collected
60 from the debris at the base of an outcrop of kyanite-bearing migmatitic paragneiss (lower part
61 of Unit 1), located close to Titar village (North of Dana village, Fig. 1b). In this outcrop,
62 gneisses have a porphyroblastic texture and contain quartz + plagioclase + biotite + garnet +
63 kyanite + white mica (Fig. 2a). Monazite, xenotime, apatite, zircon, tourmaline, rutile,
64 ilmenite and pyrite are present as accessory minerals. Ilmenite is present in the matrix,
65 whereas rutile occurs only as relict cores in the former mineral and within garnet and kyanite
66 (Carosi et al. 2015; Iaccarino et al. 2015). Tonalitic leucosomes, mainly made of quartz +
67 plagioclase + kyanite, occur parallel to the main foliation defined by biotite and white mica
68 (Fig. 2a; Iaccarino et al. 2015). Garnet crystals both in the rock matrix and collected at the
69 base of the outcrop contain analogous mineral and melt inclusions and show exactly similar
70 compositional features (Carosi et al. 2015; Iaccarino et al. 2015), indicating that the dispersed
71 investigated garnet come from adjacent Ky-bearing migmatites.

72 Phase equilibria modeling of migmatitic paragneisses indicates peak conditions of
73 710–720 °C and 1.0–1.1 GPa, whereas the application of Zr-in-rutile thermometer yielded
74 temperatures of \approx 650–720 °C (at P=1.1 GPa), interpreted as prograde temperatures (Fig. 2b;
75 Iaccarino et al. 2015). These rocks underwent anatexis with the subsequent formation of
76 leucosomes close to peak conditions, and then decompression and cooling to 650–670 °C and

77 0.7-0.8 GPa (Iaccarino et al. 2015). The calculated amount of melt generated at peak
78 conditions is ≈ 7.5 vol% (Fig. 2b), approaching the critical threshold for melt interconnection
79 and migration (≈ 7 vol%; Rosenberg and Handy 2005). As a matter of fact, melt accumulation
80 is observed in leucosomes and in dilational structures, whose total volume is far more than
81 the predicted amount of melt at peak conditions (Fig. 2a) (see Iaccarino et al. 2015).

82 In situ U–Th–Pb dating of monazite has constrained the partial melting process at c.
83 41–28 Ma (Fig. 2b; Carosi et al. 2015; Iaccarino et al. 2015). On the basis of these and
84 previous geochronological constraints, crustal anatexis in the kyanite stability field in Kali
85 Gandaki valley, and in general in central and eastern Nepal, was ascribed to the
86 underthrusting of the GHS beneath THS following continental collision (Carosi et al. 2015).

88 **Nanogranitoid inclusions**

89 The investigated garnet is 10 mm in diameter and contains hundreds of nanogranitoid
90 inclusions showing a systematic distribution in an annulus located in an intermediate position
91 between core and rim (Fig. 3a, b). Nanogranitoids are 10–20 μm in size, often show an
92 irregular shape and coexist with tiny single mineral inclusions of ilmenite, rutile, apatite,
93 zircon and monazite (Fig. 3c-f). These minerals also appear within melt inclusions (Fig. 3f)
94 and represent accidental trapped phases, as suggested by their relative large size compared
95 with the size of the inclusions, by their low solubility in crustal melts and by the presence of
96 indentations within the inclusion walls (e.g., Cesare and Maineri 1999; Barich et al. 2014).
97 Kyanite is not present as mineral inclusions within the investigated garnet, as already
98 observed for other garnet porphyroblasts occurring in Ky-bearing migmatites from this area
99 (Carosi et al. 2015). Cryptocrystalline aggregates of quartz + plagioclase + muscovite +
100 chlorite \pm biotite commonly constitute nanogranitoids (Fig. 3c-f; see also Carosi et al. 2015),
101 suggesting the former presence of a Si- and Al-rich melt. Experimental re-homogenization

102 via piston cylinder apparatus at 800 °C (see details in Bartoli et al. 2013b) has confirmed the
103 granitoid and peraluminous composition of the trapped melt ($\text{SiO}_2 > 65$ wt%, $\text{FeO} \approx 2\text{--}3$ wt%,
104 $\text{CaO} \approx 1\text{--}4$ wt%, $\text{Na}_2\text{O} \approx 1\text{--}4$ wt%, $\text{K}_2\text{O} \approx 0.3\text{--}2$, $\text{P}_2\text{O}_5 \approx 0.2$ wt% $\text{ASI} \geq 1.3$; Carosi et al. 2015;
105 Cesare et al. 2015).

106

107 **Analytical methods**

108 Trace elements in natural (experimentally untreated) and unexposed inclusions beneath
109 garnet surface (Table 1) have been analyzed at the Department of Earth Sciences, ETH
110 Zürich by laser ablation inductively coupled plasma mass spectrometry (LA-ICPMS) using a
111 GeoLas system for ablation coupled to an Element XR (Thermo Fisher, Germany). The glass
112 NIST SRM 610 was employed as external standard. The acquired time-resolved signals were
113 processed using the software SILLS (Guillong et al. 2008). Owing to the small size of
114 nanogranitoids, also part of the host garnet has been ablated along with target inclusions.
115 Therefore, the deconvolution of the resulting mixed garnet-glass signal was applied following
116 the procedure of Halter et al. (2002). The Na_2O and FeO contents determined by EMP were
117 used as reference standards for inclusion and garnet, respectively. For elements enriched in
118 the inclusion, the concentrations is accurate within 20 to 40%. Elements which are strongly
119 compatible in the host garnet (HREE, Y) are normally not detectable in the inclusions due to
120 the dominance of the host signal and were not collected. Gd, V, Zn and Sc show substantially
121 higher contents in the host garnet than in nanogranitoids (Table 1). Therefore, the amount of
122 these elements cannot be reliably estimated in the inclusions. Some inclusions show
123 anomalous very high concentrations of Zr, Th, U, Hf and Nb, suggesting the occurrence of
124 accidental trapped phases (e.g., zircon, monazite, rutile and ilmenite). For these inclusions,
125 only the content of Li, B, Rb, Sr, Ba was reported in Table 1 and discussed in the text.

126 The H_2O measurements of re-homogenized melt (i.e., glassy) inclusions (Table 2) were

127 performed using the Cameca Nano Secondary Ion Mass Spectrometry 50 (NanoSIMS)
1
2 128 installed at Muséum National d'Histoire Naturelle (Paris). Polished experimental capsules
3
4 129 with glassy inclusions exposed on the garnet surface and standard glasses were mounted in
5
6
7 130 indium (Aubaud et al. 2007). Inclusions were identified by collecting secondary ion images
8
9
10 131 of Si, Al, K and Fe. For each analysis location, a pre-sputtering step on a $3 \times 3 \mu\text{m}^2$ surface
11
12 132 area was firstly done for 2 minutes with a 360 pA primary Cs^+ beam to remove the gold
13
14 133 coating, surface contamination and to reach a steady state sputtering regime (Thomen et al.
15
16
17 134 2014). Then a primary beam of 60 pA was used for data acquisition. Data were acquired by
18
19 135 rastering a $3 \times 3 \mu\text{m}^2$ surface area and collecting ions only from the inner $1 \times 1 \mu\text{m}^2$ (using the
20
21
22 136 beam blanking mode) to reduce surface and redeposition contamination. In order to
23
24 137 compensate charging effects, the electron gun was used while pre-sputtering and collecting
25
26 138 time. Each analysis is a stack of 200 cycles, a cycle being 1.024s long. $^{16}\text{OH}^-$ (used as a proxy
27
28
29 139 for H_2O), $^{28}\text{Si}^-$, $^{39}\text{K}^{16}\text{O}^-$ and $^{56}\text{Fe}^{16}\text{O}^-$ were recorded simultaneously in multicollection mode.
30
31 140 We checked that $^{16}\text{OH}^-/^{28}\text{Si}^-$ ratio was stable during analyses. Secondary ions were collected
32
33
34 141 by electron multipliers with a dead time of 44 ns. Mass resolution was set to 8000, enough to
35
36 142 resolve isobaric interference on $^{16}\text{OH}^-$. For NanoSIMS calibration we used granitic glasses
37
38
39 143 showing different H_2O contents (for details on calibration procedure and correction curve see
40
41 144 Bartoli et al. 2014). Data corrections, using the aforementioned calibration, and error
42
43
44 145 calculations were performed using the R program. Errors combine counting statistic and
45
46 146 uncertainty of the calibration curve. However, the errors reported in Table 2 are dominated
47
48
49 147 by the uncertainty of the calibration curve, which corresponds to prediction interval at 68%.
50
51 148 During the session, the vacuum in the analysis chamber remained between 2.5 and 5×10^{-10}
52
53 149 Torr.
54
55
56 150
57
58 151
59
60
61
62
63
64
65

152 Results

1
2
3 153 Melt inclusions show highly variable concentrations of typical incompatible elements
4
5 154 such as Li (40–400 ppm), B (200–3400 ppm), Rb (40–400 ppm), Sr (5–100) and Ba (30–900
6
7 155 ppm) (Table 1). The contents of elements typically controlled by the dissolution of accessory
8
9 156 minerals are very low (Zr= 3–8 ppm; Th=0.1–1.2 ppm; LREE=4–11 ppm). U ranges from 1
10
11
12 157 to 8 ppm. The Nb/Ta and U/Th ratios are 3–15 and 3–21, respectively. Nanogranitoids also
13
14
15 158 contain appreciable amounts of Sc (3–76 ppm), V (0.4–20 ppm) and Zn (14–92 ppm), though
16
17 159 these concentrations might be affected by contamination from the host (see above and Fig.
18
19
20 160 5a). When compared with the composition of the upper continental crust, nanogranitoids
21
22 161 from Kali Gandaki are enriched in Pb, Li and B, and depleted in Ba, Th, Nb, LREE, MREE,
23
24
25 162 Sr, Zr and Hf (Fig. 4a). On the other hand, Rb, U and Ta show variable degrees of enrichment
26
27 163 and depletion. In the chondrite-normalized diagram, melt inclusions show weak to moderate
28
29
30 164 positive Eu anomalies ($\text{Eu}/\text{Eu}^* = 1.2\text{--}3.3$) (Fig. 4b).

31
32 165 The H₂O concentrations of the re-homogenized nanogranitoids determined by
33
34 166 NanoSIMS span a relatively wide range of values from 6.5 to 10.5 wt%, with one single
35
36
37 167 value up to 14.4 wt% (mean value of 8.9 ± 1.8 wt%; Fig. 5 and Table 2). Melt inclusions
38
39 168 were too small to perform replicated analyses within a single inclusion. However, the
40
41
42 169 distribution of H₂O is expected to be quite homogeneous in glassy inclusions obtained from
43
44 170 remelting experiments (Bartoli et al. 2014; Acosta-Vigil et al. 2016). H₂O estimated by
45
46 171 difference of electron microprobe totals from 100% yielded similar mean content (9.6 ± 1.4
47
48
49 172 wt%) compared to the NanoSIMS mean data (Fig. 5).

50
51 173 Figure 6 shows zircon and monazite saturation temperatures (T_{Zrn} and T_{Mnz} ,
52
53
54 174 respectively) for investigated melt inclusions, calculated following methods proposed by
55
56 175 Watson and Harrison (1984), Montel (1993) and Stepanov et al. (2012). T_{Zrn} and T_{Mnz} were
57
58
59 176 calculated from nanogranitoids not containing accidental trapped minerals; we carefully
60
61
62
63
64
65

177 avoided considering any data coming from analyses of nanogranitoids containing trapped
178 mineral inclusions such zircon or monazite (see above). T_{Zm} values vary from 541 to 594 °C.
179 The two different calibrations for the T_{Mnz} thermometer provide different temperature ranges
180 such as 544–650 °C (Montel 1993) and 412–533 °C (Stepanov et al. 2012).

181

182 **Phase equilibria modeling**

183 Migmatites from Kali Gandaki valley have been already investigated by means of phase
184 equilibria modeling (Iaccarino et al. 2015). In this contribution this approach was instead
185 applied considering only the average bulk composition of remelted nanogranitoids to
186 compare the predicted subsolidus mineral assemblages with those observed in the crystallized
187 melt inclusions. The average H₂O content was estimated by EMP-difference and is consistent
188 with the NanoSIMS values (Fig. 5). Calculations were performed in the Na₂O–CaO–K₂O–
189 FeO–MgO–Al₂O₃–SiO₂–H₂O (NCKFMASH) chemical system, using Perple_x software
190 version 6.8.3. Considering the pitfalls and uncertainties related to phase equilibria approach
191 (White et al. 2011; Bartoli et al. 2013c, 2016b; Forshaw et al. 2019) two P – T sections were
192 calculated for the same bulk composition, one using the internally consistent dataset hp04ver
193 (Holland and Powell 2003) and the older activity–composition (a–x) models, and another
194 calculated using dataset hp11ver (Holland and Powell 2011) and the re-parameterized a–x
195 models. The following a–x relations were selected. For hp11ver: melt, garnet, chlorite,
196 orthopyroxene, muscovite, biotite and cordierite from White et al. (2014), ilmenite from
197 White et al. (2000), plagioclase and K-feldspar from Holland & Powell (2003). For hp04ver:
198 melt from White et al. (2007), garnet, orthopyroxene and chlorite from Holland and Powell
199 (1998), biotite from Tajčmanová et al. (2009), white mica from Coggon and Holland (2002),
200 plagioclase from Newton et al. (1980) and K-feldspar from Thompson and Hovis (1979). An
201 ideal model was used for cordierite and ilmenite. In all calculations pure phases included

202 quartz, rutile, kyanite, sillimanite, andalusite and aqueous fluid.

203 The overall topology of the two P - T sections appears somewhat different, but there
204 are not important variations in terms of phase assemblages (Fig. 7). Modeling of the bulk
205 composition for the investigated nanogranitoids shows the appearance of melt at $T > 680$ - 690
206 $^{\circ}\text{C}$ (Fig. 7). The subsolidus field is occupied by variable mineral assemblages which are
207 mainly characterized by the presence of chlorite, biotite, muscovite, paragonite, garnet,
208 plagioclase and quartz. At <500 $^{\circ}\text{C}$ and <0.4 GPa, the predicted stable mineral assemblages
209 are quartz + plagioclase + muscovite + chlorite + biotite and quartz + plagioclase +
210 muscovite + chlorite (Fig. 7). These assemblages resemble those observed in many
211 nanogranitoid inclusions (see above). Some pores observed during SEM analysis (Fig. 3)
212 likely reflect the former presence of volatiles (in particular H_2O) in excess to the amounts
213 used by phyllosilicates and therefore exsolved during melt crystallization (see Bartoli et al.
214 2013a), in agreement with free H_2O predicted by the model at subsolidus conditions (Fig. 7).
215 In addition, the model indicates that chlorite is likely to be a phase formed in the subsolidus
216 during cooling, whose formation did not involve infiltration of external fluids (i.e., the
217 presence of chlorite in nanogranitoids does not imply that melt inclusions have been modify
218 by late stage fluid alteration). This finding is also consistent with the coexistence of chlorite
219 and unaltered biotite in nanogranitoids from Ivrea Zone (Carvalho et al., 2018).

220

221 **Discussion**

222 **Nanogranitoids represent primary prograde Eohimalayan crustal melts**

223 Their microstructural distribution, together with the experimental re-homogenization, major
224 and trace element compositions and H_2O contents, and results from phase equilibria modeling
225 (Carosi et al. 2015 and this work), confirm that these polycrystalline inclusions represent
226 former primary melt droplets that have crystallized into a cryptocrystalline aggregate; that is,

227 they are nanogranitoids (Cesare et al. 2015; Bartoli et al. 2016a). Their systematic
1
2 228 distribution in an annulus around the garnet core points to a primary origin (Roedder 1979),
3
4
5 229 implying that they were trapped by garnet during its growth. Therefore, the portion of garnet
6
7 230 containing melt inclusions certainly formed in the presence of an anatectic melt during
8
9
10 231 incongruent melting (i.e., this portion has certainly a peritectic origin: Cesare et al. 2015).
11
12 232 This is consistent with the increase of garnet mode (5 to 9 vol%; Iaccarino et al. 2015)
13
14 233 predicted by the modeling at the temperature of melting (Fig. 2b). The formation of peritectic
15
16 234 garnet at ≤ 700 °C might appear problematic, but it was already documented in Ronda
17
18
19 235 metatexites (S Spain), where it was interpreted as the consequence of a continuous melting
20
21
22 236 reaction consuming biotite (Bartoli et al. 2013c). Also, geochemical signatures typical of
23
24 237 muscovite melting were found in melt inclusions hosted in peritectic garnet from El Hoyazo
25
26
27 238 anatectic enclaves (SE Spain), indicating that this peritectic mineral likely grew (and trapped
28
29 239 melt droplets) through melting reactions consuming Fe-bearing muscovite at around 700-750
30
31
32 240 °C (Acosta-Vigil et al. 2010).

33
34 241 The investigated garnet has been collected at the base of a rock wall made of Ky-
35
36 242 bearing, partially- melted gneiss. Rocks from this outcrop have been intensively studied in
37
38
39 243 the recent years. On the basis of thermodynamic modeling, peritectic garnet likely grew in
40
41 244 the presence of a melt phase from 650 to 720 °C, at 1.0–1.1 GPa (Fig. 2b; Iaccarino et al.
42
43
44 245 2015). In situ U–Th–Pb dating of monazite grains from rock matrix and included in melt
45
46 246 inclusion-bearing garnets indicates the beginning of anatexis at c. 41–36 Ma (Fig. 2a; see also
47
48
49 247 Carosi et al. 2015). Near peak-pressure melting has been dated at c. 36–28 Ma by Iaccarino et
50
51 248 al., (2015). These geochronological constraints are in agreement with the age of c. 35 Ma
52
53
54 249 obtained by U–Pb monazite and zircon dating of a Ky-bearing leucosome collected close to
55
56 250 Taglung, 10-12 km from the Titar village (Godin et al. 2001).

57
58 251 Considering their primary origin and the geochronological constraints reported above,
59
60
61
62
63
64
65

252 it is reasonable to interpret that the investigated nanogranitoids reflect primary anatectic
1
2 253 melts produced during the Eocene-Early Oligocene (Eohimalayan) prograde metamorphism
3
4
5 254 associated to crustal thickening during the early stages of the India–Asia collision.
6

7 255

10 256 **Conditions and mechanisms of Eohimalayan anatexis in Kali Gandaki**

12 257 Most re-homogenized nanogranitoids from Kali Gandaki valley are granodiorites,
13
14 258 tonalites and trondhjemites, and minor granites, showing low K₂O contents (< 2.5 wt%),
15
16 259 moderate to very high Na₂O/K₂O ratio (1.1-14.1) and CaO up to 4 wt% (Carosi et al., 2015;
17
18
19 260 Bartoli et al., 2016a; Fig. 8). Notably, leucosomes in Kali Gandaki gneisses exhibit a tonalitic
20
21 261 composition (Iaccarino et al. 2015). These peculiar compositions resemble those of
22
23
24 262 experimental melts produced during H₂O-present melting of metasedimentary rocks (Fig. 8).
25
26
27 263 For instance, Patiño Douce and Harris (1998) experimentally remelted two GHS schists from
28
29 264 the hanging wall of the Main Central Thrust. Melts produced by dehydration melting of mica
30
31 265 at >750 °C (0.6-1.0 GPa) are granitic in compositions (Na₂O/K₂O = 0.7–0.9, one value up to
32
33
34 266 1.4). Instead, near-solidus melts formed at <750 °C by H₂O-present melting of muscovite
35
36 267 correspond to trondhjemites (Na₂O/K₂O = 1.4–3.9, one value of 0.9). The Na₂O/K₂O > 1 of
37
38
39 268 melt has been ascribed to the decreasing temperature of quartz + plagioclase solidus with
40
41 269 increasing H₂O amount (Patiño Douce and Harris 1998; García-Casco et al. 2003). The weak
42
43
44 270 to moderate positive Eu anomaly of Kali Gandaki nanogranitoids (Fig. 4b) would support the
45
46 271 role of plagioclase in melting reaction (Gao et al. 2017). Therefore, based on the major
47
48
49 272 element compositions of rehomogenized nanogranitoids, the presence of an aqueous fluid
50
51 273 phase during the associated anatexis could be proposed.
52

53 274 The peculiar Na-rich composition of Kali Gandaki nanogranitoids with respect to
54
55
56 275 classic granitic s.s. anatectic melts cannot be the result of melt-garnet interaction during
57
58 276 experimental remelting at temperature (800 °C) higher than that of entrapment (650-720 °C),
59
60
61
62
63
64
65

277 because the host mineral is virtually Na-free. Rather, this discrepancy is likely to be related to
1
2 278 kinetics (see below).
3

4
5 279 Rehomonized nanogranitoids have high H₂O concentrations (6.5-10.5, one value up
6
7 280 to 14.4 wt%; Fig. 5). This range approximates the expected minimum and maximum H₂O
8
9 281 contents for anatectic melts produced at these P–T conditions (≈6.5-15 wt%; Holtz et al.,
10
11 282 2001). The H₂O content approaching the maximum solubility value (≈15 wt.% at 1.1 GPa)
12
13 283 was found in a single nanogranitoid inclusion and it would be consistent with partial melting
14
15 284 under fluid-present conditions at the H₂O-saturated solidus. The lower H₂O concentrations
16
17 285 may reflect different processes. 1) Weinberg and Hasalová (2015b) argue that in the case of a
18
19 286 rock-buffered system (i.e., a system characterized by a high rock/fluid ratio) the H₂O-fluxed
20
21 287 melting would produce H₂O-undersaturated melts and that the H₂O contents would range
22
23 288 between the minimum and maximum values. 2) Alternatively, different buffering
24
25 289 assemblages at the micro-scale may be responsible for variable melt H₂O content. Bartoli et
26
27 290 al. (2014) documented that melt inclusions trapped in different garnet crystals in Ronda
28
29 291 migmatites (Spain) showed variable H₂O content and interpreted these heterogeneities as the
30
31 292 result of melt formation under conditions of “mosaic equilibrium” affecting the activity of
32
33 293 H₂O in the coexisting fluid phase and/or the solid assemblages. This explanation seems to be
34
35 294 highly improbable for Kali Gandaki sample where the distance among analyzed
36
37 295 nanogranitoids is in the order of a few hundreds of μm. 3) The loss of H₂O after melt
38
39 296 inclusion entrapment and/or during remelting experiments cannot be excluded *a priori*,
40
41 297 considering the presence of cracks in some inclusions (Fig. 3c). However, a systematic loss
42
43 298 of H₂O from nanogranitoids during subsolidus retrograde history is expected to result in a
44
45 299 larger variability of the melt H₂O contents, with compositions approaching dry values. This is
46
47 300 not the case here, where the majority of melt H₂O contents define a relatively narrow range,
48
49 301 never below 6.5 wt% (Fig. 5).
50
51
52
53
54
55
56
57
58
59
60
61
62
63
64
65

302 One could argue that H₂O loss after melt inclusion entrapment could partly explain
1
2 303 the discrepancy between the trapping temperature and the temperature at which
3
4 304 nanogranitoids were experimentally remelted (800 °C). However, again, this discrepancy
5
6
7 305 may be explained without taking into account the loss of H₂O. Indeed, higher remelting
8
9
10 306 temperatures could be needed because melting kinetics play a fundamental role during
11
12 307 reheating experiments. Smaller inclusions usually remelt more rapidly than larger ones
13
14 308 (Thomas and Klemm 1997) and nanogranitoids from Kali Gandaki show larger size than melt
15
16
17 309 inclusions for which a run duration of 24 h was tested (Bartoli et al., 2013c and discussion
18
19 310 therein). Therefore, a process of H₂O loss affecting the majority of analyzed inclusions does
20
21
22 311 not seem to be supported by convincing evidence.
23

24 312 To summarize, the occurrence of near H₂O-saturated melts would support a H₂O-
25
26 313 present melting scenario, confirming the inferences based on major element compositions of
27
28
29 314 nanogranitoids and temperature estimates of Kali Gandaki migmatites (see above). The
30
31 315 observed H₂O variability, which is likely to be primary and ranges between the expected
32
33
34 316 minimum and maximum values, would suggest the existence of a H₂O-present, rock-buffered
35
36 317 system during Eohimalayan anatexis. These observations are consistent with anatexis and
37
38
39 318 melt formation in the proximity of the H₂O-saturated solidus (Fig. 2).
40

41 319 T_{Zrn} and T_{Mnz} are ≈ 100 - 250 °C lower than suprasolidus temperatures obtained for
42
43 320 migmatites collected in the same area (Fig. 6). T_{Zrn} and T_{Mnz} values are also notably lower
44
45
46 321 than the minimum temperature at which crustal protoliths melt in the presence of an aqueous
47
48
49 322 fluid (≈ 650 °C). Migmatites from Kali Gandaki valley contain abundant grains of zircon and
50
51 323 monazite occurring in matrix as well as in garnet, kyanite, biotite and quartz (Carosi et al.
52
53 324 2015; Iaccarino et al. 2015). In addition, these accessory minerals are present as accidentally
54
55
56 325 trapped phases within some nanogranitoids (Fig. 3d, f). One, therefore, could assume that
57
58 326 melt pockets were likely in contact with zircon and monazite during the early stages of
59
60
61
62
63
64
65

327 melting. Because zircon and monazite are expected to break down and dissolve at
1
2 328 suprasolidus conditions during prograde metamorphism to maintain saturation of the melt
3
4 329 (Yakymchuk and Brown 2014; Yakymchuk 2017), the undersaturated composition of melt
5
6
7 330 inclusions with respect to the accessory minerals would suggest a limited time of interaction
8
9
10 331 between zircon/monazite and anatectic melt. On the other hand, the amount of melt was
11
12 332 likely low (around the percolation threshold; Fig. 2) and, therefore, the lack of contact with
13
14 333 accessory phases cannot be excluded. In any case, the very low T_{Zm} and T_{Mnz} values have to
15
16
17 334 be ascribed to the lack of equilibration between melt pockets and accessory minerals present
18
19 335 in the rock. Some degrees of disequilibrium involving accessory minerals and melt inclusions
20
21
22 336 in anatectic rocks have been already documented during the entrapment of low-temperature
23
24 337 (<750 °C) melt droplets in El Hoyazo metapelitic enclaves (Acosta-Vigil et al. 2010). In that
25
26
27 338 case, a much smaller difference of 25-50 °C between calculated and expected temperatures
28
29 339 has been reported (see discussion in Acosta-Vigil et al. 2012).

31
32 340 To date, the most complete dataset of trace element compositions of melt inclusions
33
34 341 from metapelitic anatectic rocks is that presented by Acosta-Vigil et al. (2010, 2012). In
35
36 342 residual anatectic enclaves within peraluminous dacites of the Neogene Volcanic Province
37
38
39 343 (NVP) of SE Spain, a systematic evolution of trace element content of anatectic melt
40
41 344 (recorded as melt inclusions in several minerals and as matrix glass) is observed. Combining
42
43
44 345 microstructural and geochemical data, these authors interpreted that concentrations in melt of
45
46 346 Li, Cs and B decrease whereas those of Zr, Th, REE, V, Cr, Co, Zn increase with increasing
47
48
49 347 melting temperature, due to the consumption of muscovite (main carrier of Li, B and Cs) at
50
51 348 low temperature and biotite (main reservoir of Rb) and accessory phases (LREE, Zr, Hf, U,
52
53
54 349 Th) at higher temperature (Acosta-Vigil et al. 2010). These authors interpreted the melt
55
56 350 inclusions in plagioclase and garnet to represent crustal melts formed by the H₂O-present to
57
58 351 H₂O-absent muscovite melting reactions, whereas the matrix glass formed by biotite fluid-

352 absent melting (see also Acosta-Vigil et al. 2017).

1
2 353 The majority of investigated nanogranitoids from Kali Gandaki valley show higher B
3
4
5 354 content, similar Li concentration and Rb/Sr ratio, and lower Ba, Ce, Th, Zr, Hf and Rb/B
6
7 355 values with respect to NVP melts produced at ≤ 750 °C (Fig. 9). The U/Th ratio is variable,
8
9
10 356 from values approaching those observed in El Hoyazo low-temperature melts up to much
11
12 357 greater contents (> 10 ; Fig. 9g), suggesting that Kali Gandaki nanogranitoids could reflect the
13
14
15 358 composition of the first melt produced. All these compositional features are consistent with i)
16
17 359 melting at low temperature and ii) the undersaturation of melt with respect to the accessory
18
19 360 minerals (see above). Two melt inclusions from the investigated garnet display very high Ba
20
21
22 361 amount (> 600 ppm; Fig. 9c). The high B contents (Fig. 9a, b) may point to the presence and
23
24 362 dissolution of tourmaline during the melt-producing reaction. Indeed, this mineral is a
25
26
27 363 common accessory phase in Ky-bearing gneisses from this area (Iaccarino et al. 2015). Wolf
28
29 364 and London (1997) experimentally demonstrated that at the onset of crustal melting
30
31
32 365 tourmaline breaks down incongruently to assemblages containing Al-, Fe- and/or Mg-bearing
33
34 366 solid phases (i.e., garnet, biotite, sillimanite) and a B-enriched melt. Alternatively, the
35
36
37 367 infiltration of B-rich fluids into the anatectic zone and formation of B-enriched melts cannot
38
39 368 be ruled out (Acosta et al. 2001; and references therein) and it would be consistent with a
40
41 369 melting scenario characterized by the presence of an aqueous fluid (see above).

42
43
44 370 Acosta-Vigil et al. (2012) modeled REE abundance in crustal melts of El Hoyazo
45
46 371 considering different scenarios (e.g., disequilibrium melting of feldspars, equilibrium
47
48
49 372 dissolution of accessory phases and equilibrium with major and accessory minerals).
50
51 373 Similarly, Prince et al. (2001) calculated REE profiles of crustal melts derived from GHS
52
53
54 374 metapelites assuming that REE abundances are controlled by accessory phase dissolution and
55
56 375 by disequilibrium melting of plagioclase. Collectively these calculations indicate that REE-
57
58 376 poor melts with a strong positive Eu anomaly can be due to the disequilibrium melting of
59
60
61
62
63
64
65

377 feldspars, whereas dissolution of accessory phases results in higher REE contents and
378 negative Eu anomalies (Fig. 10). The REE pattern and positive Eu anomalies of Kali Gandaki
379 nanogranitoids resemble those of El Hoyazo melt inclusions hosted in garnet and models
380 based on the dissolution of feldspars, and differ significantly from models associated with the
381 dissolution of accessory minerals (Fig. 10). Therefore, it follows that the latter process is not
382 likely responsible for the REE abundances of nanogranitoids. Also, the extremely variable,
383 LREE concentrations in melt suggest the lack of equilibration between melt and residue.

384

385 **Eohimalayan anatexis and granitoid formation**

386 Kyanite-bearing migmatitic gneisses of the lower GHS in the Kali Gandaki valley underwent
387 low temperature (up to 720 °C) Eocene to Early Oligocene anatexis, with the formation of
388 low amounts of melt (≈ 7.5 vol.%; Fig. 2b) at peak conditions (Carosi et al. 2015; Iaccarino et
389 al. 2015). However, similar rocks, which represent significant portions of the metamorphic
390 core of the Himalayas, experienced higher temperatures and/or higher melting degrees in
391 other localities of GHS, between Eocene and Late Oligocene.

392 For example, the Ky-bearing migmatites in the Main Central Thrust Zone (Arun
393 valley, eastern Nepal Himalaya) reached peak conditions at 820 °C and 1.3 GPa, during Early
394 Oligocene (≈ 31 Ma), producing ≈ 15 vol.% melt (Groppo et al. 2010). Guilmette et al. (2011)
395 reported peak conditions of 820 °C and > 1.4 GPa for Ky-bearing anatectic paragneisses from
396 the Namche Barwa (Eastern Himalayan Syntaxis). Here partial melting is considered to have
397 generated 20–23 vol.% total melt. The HP metamorphism was dated at 37–32 Ma (Zhang et
398 al. 2010). Zhang et al. (2015) documented melting of pelitic granulites from the same area
399 (Namche Barwa Complex) at peak conditions of 840–880 °C and 1.3–1.6 GPa; anatexis of
400 these rocks produced up to ≈ 30 vol.% melt from c. 40 to 30 Ma. Here metagreywackes
401 reached peak conditions of 820–845 °C and 1.5–1.6 GPa (Tian et al. 2016). Palin et al. (2014)

1
2
3
4
5
6
7
8
9
10
11
12
13
14
15
16
17
18
19
20
21
22
23
24
25
26
27
28
29
30
31
32
33
34
35
36
37
38
39
40
41
42
43
44
45
46
47
48
49
50
51
52
53
54
55
56
57
58
59
60
61
62
63
64
65

402 dated the melting at ≈ 700 °C and ≈ 1.0 GPa in the northwestern flank of the Eastern
403 Himalayan Syntaxis between c. 44 and 33 Ma. Leucosomes in Ky-bearing migmatites
404 comprise up to 20% of the outcrop and formed as a result of Kfs-absent, fluid present melting
405 reactions. In the Kharta Area (Southern Tibet) metasedimentary migmatites experienced
406 anatexis conditions of 750–800 °C and 1.4 GPa, at ≈ 33 Ma (Liu et al. 2007). Phase equilibria
407 modeling demonstrated that Barun gneisses (Eastern Nepal) reached peak conditions of 800–
408 850 °C in the kyanite field, with the formation of 15–20 vol.% melt (Groppo et al. 2012).
409 Melting at the bottom of the GHS (e.g., Barun gneisses) was dated at 33–28 Ma (Carosi et al.
410 2015 and references therein).

411 Considering their low melting temperature and degree, Kali Gandaki anatexis
412 gneisses probably did not act as source region of voluminous anatexis melts. However, from
413 the above, it is clear that Ky-bearing migmatites have played an important role during
414 Eohimalayan anatexis. As a matter of fact, melting of metasedimentary lithologies from GHS
415 is considered to have contributed to the granitoid magmatism occurred during crustal
416 thickening at variable temperatures and under variable fluid regimes (Prince et al. 2001; Zeng
417 et al. 2009; 2011; Aikman et al. 2012). Therefore, nanogranitoids from Kali Gandaki gneisses
418 may provide us with a snapshot of anatexis melts whose extraction from similar lithologies
419 and emplacement at shallower levels have resulted in the formation of Eohimalayan
420 granitoids.

421 Granitic to trondhjemitic bodies from the upper GHS of Garhwal Himalaya are
422 considered to be derived from H₂O-present melting of Ky-bearing GHS metasedimentary
423 rocks at 650 °C during Eohimalayan prograde metamorphism (39 ± 3 Ma) (Prince et al.
424 2001). These Eohimalayan granitoids, which differ from the classic Miocene leucogranites,
425 share some key features with the Kali Gandaki melt inclusions, such as Ca- and Na-
426 enrichment (up to 2.0 and 3.9 wt%, respectively), very low melting temperatures and a

427 positive Eu anomaly (Prince et al. 2001). In the haplogranitic Qtz-Ab-Or diagram the
1
2 428 Garhwal rocks plot in the proximity of Kali Gandaki nanogranitoids and experimental glasses
3
4
5 429 produced via H₂O-present melting (Fig. 8). Anatectic gneisses of Kali Gandaki valley may
6
7 430 reasonably be considered the analog source rocks of Eohimalayan Garhwal granitoids. Active
8
9
10 431 shear zones in this area could have facilitated the ingress of external fluids, enhancing the
11
12 432 amount of melt produced (Prince et al. 2001). Instead, a large supply of external aqueous
13
14
15 433 fluids did not occur in Kali Gandaki area where melting stopped at low degrees.

16
17 434 Granite compositions have been often interpreted in the light of “restite unmixing”
18
19 435 model (Chappell et al. 1987), which states that the majority of granites represent mixtures
20
21
22 436 between a minimum or near-minimum temperature melt and the restite (residuum), and that
23
24 437 the compositional variability in granites reflects varying degrees of restite unmixing.

25
26
27 438 The Ba and Sr content of three Garhwal granites can be modeled as the variable
28
29 439 mixture of a starting melt (represented by nanogranitoids) and a residuum composed of
30
31
32 440 variable amounts of biotite, plagioclase and K-feldspar (Fig. 9d). One rock needs solely the
33
34 441 addition of 5 vol% K-feldspar. However, the same mixtures with a biotite-bearing residuum
35
36 442 would result in Rb/Sr ratios much higher (≈ 12) than those measured (< 1 ; Fig. 9c). The very
37
38
39 443 high Ba content and very low Rb/Sr of Garhwal rocks could, instead, be explained by
40
41 444 addition of solely K-feldspar, up to 20 vol% (Fig. 9c). These mismatches clearly indicate that
42
43
44 445 entrapment of residual minerals does not explain the trace element concentrations controlled
45
46 446 by major minerals. Although the addition of very tiny amounts of zircon and monazite could
47
48
49 447 explain Ce, Th, U and Zr variability in Garhwal rocks (Fig. 9e, f), this is unlikely. Firstly, the
50
51 448 entrainment of phases from the source region is not a selective process (Sawyer 2014).
52
53
54 449 Rather, the inheritance of accessory minerals should be coupled with that of major phases in
55
56 450 which they are usually included (micas and feldspars). Again, the mixing with a biotite-,
57
58 451 feldspar-bearing residuum is highly improbable (see above). Secondly, the higher Zr, Th and
59
60
61
62
63
64
65

452 Ce contents are perfectly consistent with higher degrees of melting compared to those in Kali
1
2 453 Gandaki migmatites. Accessory phase dissolution and disequilibrium melting of plagioclase
3
4
5 454 are considered to have shaped the LREE patterns and positive Eu anomaly, respectively, of
6
7 455 Garhwal rocks (Fig. 10; Prince et al. 2001). This is mostly in agreement with the diverse La,
8
9
10 456 Ce and Eu contents of Kali Gandaki nanogranitoids whose composition seems to be
11
12 457 controlled by the dissolution of plagioclase and lack of equilibrium with accessory minerals
13
14 458 (Fig. 10).

16
17 459 Prince et al. (2001) ascribed the very high Ba content of these rocks (> 600 ppm; Fig.
18
19 460 9c) to fluid transport of Ba, which “is a well-documented phenomenon during crustal melting
20
21
22 461 (Weinberg and Searle 1999)”. Surprisingly, Ba is highly variable in Kali Gandaki
23
24 462 nanogranitoids, formed in a H₂O-present scenario (see above), with the highest contents
25
26
27 463 resembling those observed in some Garhwal rocks (Fig. 9c).

28
29 464 Summarizing, the comparison between nanogranitoids and granites indicates i) that
30
31
32 465 the restite unmixing process did not shape the composition of Garhwal rocks and that an
33
34 466 aqueous fluid was involved in melting process, reinforcing the inferences of Prince et al.
35
36 467 (2001), and ii) that Kali Gandaki melt inclusions are recording the very beginning of melting
37
38
39 468 in a scenario that, in other GHS localities, has produced Eohimalayan granitoids.

40
41 469

44 470 **Conclusions**

- 45
46 471 1. Kali Gandaki nanogranitoids occur within peritectic garnet whose formation has been
47
48
49 472 ascribed to the Eohimalayan prograde metamorphism at conditions of 650–720 °C
50
51 473 and 1.0–1.1 GPa and has been dated at c. 41–36 Ma (see Carosi et al. 2015; Iaccarino
52
53
54 474 et al. 2015).
- 55
56 475 2. During their crystallization, nanogranitoids developed a quartz + plagioclase +
57
58
59 476 muscovite + chlorite ± biotite assemblage.

- 477 3. Major element compositions and H₂O contents of rehomogenized nanogranitoids
1
2 478 suggest the presence of an aqueous fluid phase during melting, in agreement with the
3
4
5 479 inferred melting conditions.
6
7 480 4. The low Zr, Th and LREE concentrations along with the very low zircon and
8
9
10 481 monazite saturation temperatures indicate some degrees of disequilibrium between
11
12 482 accessory minerals and coexisting melt.
13
14
15 483 5. Investigated nanogranitoids are incipient melts, which did not have time to equilibrate
16
17 484 with their source rock.
18
19 485 6. Kali Gandaki nanogranitoids share some key features with Eohimalayan granitoids
20
21
22 486 from Garhwal Himalaya (i.e., major elements, very low melting temperature, Ba
23
24 487 enrichment). A comparative study supports previous inferences of Prince et al.
25
26
27 488 (2001): Garhwal rocks likely represent pristine crustal melts formed under H₂O-
28
29 489 present conditions, whose composition was not modified by entrainment of residuum.
30

31 490
32
33
34 491 **Acknowledgments** This research benefitted from funding from the Italian Ministry of
35
36 492 Education, University, Research (Progetto SIR RBSI14Y7PF), from Padova University
37
38
39 493 (Progetti per Giovani Studiosi 2013) and from Società Italiana di Mineralogia e Petrologia
40
41 494 (grant for a research stay abroad) to OB; from the CARIPARO (Cassa di Risparmio di
42
43
44 495 Padova e Rovigo) project MAKEARTH to BC. The National NanoSIMS facility at the
45
46 496 MNHN was established by funds from the CNRS, Région Ile de France, Ministère délégué à
47
48
49 497 l'Enseignement supérieur et à la Recherche, and the MNHN. Remi Duhamel is thanked for
50
51 498 his support during NanoSIMS analyses.
52

53 499
54
55
56
57
58
59
60
61
62
63
64
65

500 FIGURE and TABLE CAPTIONS

501

502 **Fig. 1** Geological sketch map of the Kali Gandaki valley (redrawn from Carosi et al. 2015)

503

504 **Fig. 2** a) Representative hand specimen of the anatectic paragneisses. b) Phase equilibria

505 modeling and P–T path of Ky-bearing gneisses from Kali Gandaki valley (redrawn from

506 Iaccarino et al., 2015). Green rectangle: temperature range from the thermometer based on Zr

507 content in rutile. C2015 and I2015: geochronological constraints from Carosi et al. (2015)

508 and Iaccarino et al. (2015), respectively

509

510 **Fig. 3** Melt inclusions in garnet from Kali Gandaki. a) plane-polarized photomicrograph of

511 the equatorial section of the investigated garnet. Dashed white lines define the annulus

512 containing nanogranitoid inclusions (redrawn after Cesare et al. 2015). b) plane-polarized

513 photomicrograph showing a cluster of polycrystalline inclusions. c-f) SEM-BSE images of

514 nanogranitoids. Red arrows: decrepitation cracks. Yellow arrows: micro- to nano-porosity.

515 Scale bar: 5 μm

516

517 **Fig. 4** Trace element and REE composition of nanogranitoid inclusions (NG) and host garnet.

518 a) Values normalized to the average upper continental crust (UCC) composition (data from

519 Rudnick and Gao 2014). b) REE patterns. Values normalized to the chondrite C1 (Sun and

520 McDonough 1989)

521

522 **Fig. 5** H₂O concentrations of nanogranitoid inclusions determined by NanoSIMS. The error

523 associated to these values is smaller than the symbol (see Table 2). White symbols: average

524 contents. The average H₂O content estimated by EMP-difference is from Cesare et al. (2015).

525 Horizontal bars are two standard deviations on average values. The number of analyses is
1
2 526 indicated next to horizontal bars
3

4
5 527
6
7 528 **Fig. 6** Monazite and zircon saturation temperatures calculated for the investigated melt
8
9 529 inclusions. Black dots: T_{Mnz} calibration of Montel (1993). White dots: T_{Mnz} calibration of
10
11 530 Stepanov et al (2012). T_{Zrn} from Watson and Harrison (1984). Grey field: anatectic
12
13 531 temperatures estimated for Kali Gandaki gneisses by Iaccarino et al. (2015)
14
15
16

17 532
18
19 533 **Fig. 7** Comparative P–T sections for nanogranitoid inclusions calculated in the NCKFMASH
20
21 534 system with two internally consistent datasets: hp04ver for (a) and hp11ver for (b). The bulk
22
23 535 composition (mol%) used for calculation is indicated in the upper right inset and represents
24
25 536 the average composition obtained by EMP. The average H_2O content was estimated by EMP-
26
27 537 difference and is consistent with the NanoSIMS values
28
29
30

31 538
32
33
34 539 **Fig. 8** Qtz-Ab-Or diagram showing the normative compositions of Kali Gandaki
35
36 540 nanogranitoids (square represents the average value). Compositions of experimental glasses
37
38 541 (PDH98: Patiño Douce and Harris 1998; GC03: García-Casco et al. 2003) and Eohimalayan
39
40 542 granites (P2001: Prince et al. 2001) are plotted for comparison
41
42
43

44 543
45
46 544 **Fig. 9** Comparison among the trace element contents (ppm) of Kali Gandaki nanogranitoids,
47
48 545 El Hoyazo melts and Eohimalayan granitoids. Ba and Sr content of melt inclusions in
49
50 546 plagioclase were not reported because these elements are depleted being compatible with
51
52 547 respect the host phase; Hf concentrations were not reported for inclusions in plagioclase in
53
54 548 the original database (see Acosta-Vigil et al. 2012). Temperature estimates correspond to
55
56 549 zircon and monazite saturation temperatures reported by Acosta-Vigil et al. (2010). Lines
57
58
59
60
61
62
63
64
65

550 track the result of melt–residuum mixing models. Tick marks on the lines reflect increments
1
2 551 of the residuum. The average composition of nanogranitoids was considered as representative
3
4 552 of the starting melt composition, except for Ba–Rb/Sr and Ba–Sr diagrams where the two Ba-
5
6
7 553 rich melt inclusions were not considered for the average value. This assumption does not
8
9
10 554 change the inferences obtained from the geochemical modeling. Mineral compositions are
11
12 555 from Acosta-Vigil et al. (2010). See text for details
13

14 556

17 557 **Fig. 10** Comparison of REE abundances of Kali Gandaki nanogranitoids, Garwhal granites
18
19 558 and low-temperature anatectic melts modelled by Prince et al. (2001) [P2001] and Acosta-
20
21 559 Vigil et al. (2012) [AAV2012]. See text for details.
22
23

24 560

27 561 **Table 1** LA-ICP-MS analyses (ppm) of melt inclusions from Kali Gandaki garnet
28

29 562

32 563 **Table 2** H₂O concentrations measured in nanogranitoids by NanoSIMS
33

34 564

36 565 **References**

- 39 566 Acosta A, Pereira MD, Shaw DM, London D (2001) Contrasting behaviour of B during
40 567 crustal anatexis. *Lithos* 56:15–31
41 568 Acosta-Vigil A, Barich A, Bartoli O, Garrido C, Cesare B, Remusat L, Poli S, Raepsaet C
42 569 (2016) The composition of nanogranitoids in migmatites overlying the Ronda peridotites
43 570 (Betic Cordillera, S Spain): the anatectic history of a polymetamorphic basement. *Contrib*
44 571 *Mineral Pet* 171:24
46 572 Acosta-Vigil A, Buick I, Cesare B, London D, Morgan GB VI (2012b) The extent of
47 573 equilibration between melt and residuum during regional anatexis and its implications for
48 574 differentiation of the continental crust: a study of partially melted metapelitic enclaves. *J*
49 575 *Petrol* 53:1319–1356
51 576 Acosta-Vigil A, Buick I, Hermann J, Cesare B, Rubatto D, London D, Morgan GB VI (2010)
52 577 Mechanisms of crustal anatexis: a geochemical study of partially melted metapelitic
53 578 enclaves and host dacite, SE Spain. *J Petrol* 51:785–821
54 579 Acosta-Vigil A, London D, Morgan VI GB, Cesare B, Buick I, Hermann J, Bartoli O (2017)
55 580 Primary crustal melt compositions: Insights into the controls, mechanisms and timing of
56 581 generation from kinetics experiments and melt inclusions. *Lithos* 286–287:454–479
57 582 Aikman AB, Harrison TM, Hermann J (2012) The origin of Eo- and Neo-himalayan
58 583 granitoids, Eastern Tibet. *J Asian Earth Sc* 58:143–157
59
60

- 584 Aubaud C, Withers AC, Hirschmann MM, Guan Y, Leshin LA, Mackwell SJ, Bell DR
1 585 (2007) Intercalibration of FTIR and SIMS for hydrogen measurements in glasses and
2 586 nominally anhydrous minerals. *Am Mineral* 92:811–828
- 3 587 Barich A, Acosta-Vigil A, Garrido CJ, Cesare B, Tajčmanová L, Bartoli O (2014)
4 588 Microstructures and petrology of melt inclusions in the anatexic sequence of Jubrique
5 589 (Betic Cordillera, S Spain): implications for crustal anatexis. *Lithos* 206–207:303–320
- 6 590 Bartoli O, Acosta-Vigil A, Ferrero S, Cesare B (2016a) Granitoid magmas preserved as melt
7 591 inclusions in high-grade metamorphic rock. *Am Mineral* 101:1543–1559
- 8 592 Bartoli O, Acosta-Vigil A, Tajčmanová L, Cesare B, Bodnar RJ (2016b) Using
9 593 nanogranitoids and phase equilibria modeling to unravel anatexis in the crustal footwall of
10 594 the Ronda peridotites (Betic Cordillera, S Spain). *Lithos* 256–257: 282–299
- 11 595 Bartoli O, Cesare B, Poli S, Acosta-Vigil A, Esposito R, Turina A, Bodnar RJ, Angel RJ,
12 596 Hunter J (2013b) Nanogranite inclusions in migmatitic garnet: behavior during piston
13 597 cylinder re-melting experiments. *Geofluids* 13:405–420
- 14 598 Bartoli O, Cesare B, Poli S, Bodnar RJ, Acosta-Vigil A, Frezzotti ML, Meli S (2013a)
15 599 Recovering the composition of melt and the fluid regime at the onset of crustal anatexis
16 600 and S-type granite formation. *Geology* 41:115–118
- 17 601 Bartoli O, Tajčmanová L, Cesare B, Acosta-Vigil A (2013c) Phase equilibria constraints on
18 602 melting of stromatic migmatites from Ronda (S. Spain): insights on the formation of
19 603 peritectic garnet. *J Metamorphic Geol* 31:775–789
- 20 604 Bartoli O, Cesare B, Remusat L, Acosta-Vigil A, Poli S (2014) The H₂O content of granite
21 605 embryos. *Earth Planet Sci Lett* 395:281–290
- 22 606 Brown RL, Nazarchuk JH (1993) Annapurna detachment fault in the Greater Himalaya of
23 607 Central Nepal. *Geol Soc London Sp Publ* 74:461–473
- 24 608 Carosi R, Gemignani L, Godin L, Iaccarino S, Larson KP, Montomoli C, Rai SM (2014) A
25 609 geological journey through the deepest gorge on Earth: the Kali Gandaki valley section,
26 610 west-central Nepal. *Journal of Virtual Explorer* 47 (paper 7)
- 27 611 Carosi R, Montomoli C, Iaccarino S (2018) 20 years of geological mapping of the
28 612 metamorphic core across Central and Eastern Himalayas. *Earth-Science Rev* 177:124–138
- 29 613 Carosi R, Montomoli C, Langone A, Turina A, Cesare B, Iaccarino S, Fascioli L, Visonà D,
30 614 Ronchi A, Rai SM (2015) Eocene partial melting recorded in peritectic garnets from
31 615 kyanite-gneiss, Greater Himalayan Sequence, central Nepal. *Geol Soc London Sp Publ*
32 616 412:111
- 33 617 Carvalho BB, Bartoli O, Ferri F, Cesare B, Ferrero F, Remusat L, Capizzi L, Poli S (2018)
34 618 Anatexis and fluid regime of the deep continental crust: new clues from melt and fluid
35 619 inclusions in metapelitic migmatites from Ivrea Zone (NW Italy). *J Metamorphic Geol*,
36 620 DOI: 10.1111/jmg.12463
- 37 621 Carvalho BB, Sawyer EW, Janasi VA (2016) Crustal reworking in a shear zone:
38 622 transformation of metagranite to migmatite. *J Metamorphic Geol* 34:237–264
- 39 623 Carvalho BB, Sawyer EW, Janasi VA (2017) Enhancing maficity of granitic magma during
40 624 anatexis: entrainment of infertile mafic lithologies. *J Petrol* 58:1333–1362
- 41 625 Cesare B, Maineri C (1999) Fluid-present anatexis of metapelites at El Joyazo (SE Spain):
42 626 constraints from Raman spectroscopy of graphite. *Contrib Mineral Pet* 135:41–52
- 43 627 Cesare B, Acosta-Vigil A, Bartoli O, Ferrero S (2015) What can we learn from melt
44 628 inclusions in migmatites and granulites? *Lithos* 239:186–216
- 45 629 Chappell BW, White AJR, Wyborn D (1987) The importance of residual source material
46 630 (Restite) in granite petrogenesis. *J Petrol* 28:1111–1138
- 47 631 Coggon R, Holland TJB (2002) Mixing properties of phengitic micas and revised garnet–
48 632 phengite thermobarometers. *J Metamorphic Geol* 20:683–696
- 49 633 Davidson C, Grujic DE, Hollister LS, Schmid SM (1997) Metamorphic reactions related to

- 634 decompression and synkinematic intrusion of leucogranite, High Himalayan Crystallines,
 1 635 Bhutan. *J Metamorphic Geol* 15:593–612
- 2 636 Ferrero F, Angel (2018) Micropetrology: Are inclusions grains of truth? *J Petrol* 59:1671–
 3 637 1700
- 4 638 Forshaw JB, Waters DJ, Pattison DRM, Palin RM, Gopon PA (2019) Comparison of
 5 639 observed and thermodynamically predicted phase equilibria and mineral compositions in
 6 640 mafic granulites. *J Metamorphic Geol* 37:153–179
- 7 641 Gao Li-E, Zeng L, Asimow PD (2017) Contrasting geochemical signatures of fluid-absent
 8 642 versus fluid-fluxed melting of muscovite in metasedimentary sources: The Himalayan
 9 643 leucogranites. *Geology* 45:39–42
- 10 644 García-Casco A, Haissen F, Castro A, El-Hmidi H, Torres-Roldán RL, Millán G (2003)
 11 645 Synthesis of staurolite in melting experiments of a natural metapelite: consequences for
 12 646 the phase relations in low-temperature pelitic migmatites. *J Petrol* 44:1727–1757
- 13 647 Godin L (2003) Structural evolution of the Tethyan sedimentary sequence in the Annapurna
 14 648 area, central Nepal Himalaya. *J As Earth Sc* 22:307–328
- 15 649 Godin L, Parish RR, Brown L, Hodges KV (2001) Crustal thickening leading to exhumation
 16 650 of the Himalayan Metamorphic core of central Nepal: insight from U–Pb geochronology
 17 651 and ⁴⁰Ar/³⁹Ar thermochronology. *Tectonics* 20:729–747
- 18 652 Groppo C, Rolfo F, Indares A (2012) Partial melting in the Higher Himalayan Crystallines of
 19 653 Eastern Nepal: the effect of decompression and implications for the ‘Channel Flow’
 20 654 model. *J Petrol* 53:1057–1088
- 21 655 Groppo C, Rubatto D, Rolfo F, Lombardo B (2010) Early Oligocene partial melting in Main
 22 656 Central Thrust Zone (Arun valley, eastern Nepal Himalaya). *Lithos* 118:287–301.
- 23 657 Guillong M, Meier DL, Allan MM, Heinrich CA, Yardley BWD (2008) SILLS: A
 24 658 MATLAB-based program for the reduction of laser ablation ICP-MS data of
 25 659 homogeneous materials and inclusions. *Mineralogical Association of Canada Short Course*
 26 660 40, Vancouver, B.C., p. 328–333.
- 27 661 Guilmette C, Indares A, Hébert R (2011) High-pressure anatectic paragneisses from the
 28 662 Namche Barwa, Eastern Himalayan Syntaxis: textural evidence for partial melting, phase
 29 663 equilibria modeling and tectonic implications. *Lithos* 124:66–81
- 30 664 Halter WE, Pettke T, Heinrich CA, Rothen-Rutishauser B (2002) Major to trace element
 31 665 analysis of melt inclusions by laser-ablation ICP–MS: methods of quantification. *Chem*
 32 666 *Geol* 183:63–86
- 33 667 Harris N, Massey (1994) Decompression and anatexis of Himalayan metapelites. *Tectonics*
 34 668 13:1537–1546
- 35 669 Harris N, Ayres M, Massey J (1995) Geochemistry of granitic melts produced during the
 36 670 incongruent melting of muscovite: implication for the extraction of Himalayan
 37 671 leucogranite magmas: *J Geoph Res* 100:15,767–15,777
- 38 672 Harrison TM (2006) Did the Himalayan crystallines extrude partially molten from beneath
 39 673 the Tibetan Plateau? In: *Geological Constraints on Channel Flow and Ductile Extrusion as*
 40 674 *an Important Orogenic Process – Himalaya-Tibetan Plateau* (eds Law, R.D., Searle, M.P.
 41 675 & Godin, L.), Geological Society, London, Special Publication, 268:237–254
- 42 676 Hodges KV (2000) Tectonics of the Himalaya and southern Tibet from two perspectives.
 43 677 *Geol Soc Am Bull* 112:324–350
- 44 678 Hodges KV, Parrish RR, Searle MP (1996) Tectonic evolution of the central Annapurna
 45 679 Range, Nepalese Himalayas. *Tectonics* 15:1264–1291.
- 46 680 Holland TJB, Powell R (1998) An internally consistent thermodynamic data set for phases of
 47 681 petrological interest. *J Metamorphic Geol* 16:309–343
- 48 682 Holland TJB, Powell R (2003) Activity-composition relations for phases in petrological
 49 683 calculations: An asymmetric multicomponent formulation. *Contrib Mineral Pet* 145:492–

684 501

- 1 685 Holland TJB, Powell R (2011) An improved and extended internally consistent
2 686 thermodynamic dataset for phases of petrological interest, involving a new equation of
3 687 state for solids. *J Metamorphic Geol* 29(3):333–383
- 4 688 Holtz F, Johannes W, Tamic N, Behrens H (2001) Maximum and minimum water contents of
5 689 granitic melts generated in the crust: a reevaluation and implications. *Lithos* 56:1–14
- 6 690 Hu X, Garzanti E, Wang J, Huang W, An W, Webb A (2016) The timing of India–Asia
7 691 collision onset – facts, theories, controversies. *Earth-Sci Rev* 160: 264–299
- 8 692 Iaccarino S, Montomoli C, Carosi R, Massonne H-J, Langone A, Visonà D (2015) Pressure–
9 693 temperature–time–deformation path of kyanite-bearing migmatitic paragneiss in the Kali
10 694 Gandaki valley (Central Nepal): investigation of Late Eocene–Early Oligocene melting
11 695 processes. *Lithos* 231:103–121
- 12 696 Iaccarino S, Montomoli C, Carosi R, Massonne H-J, Langone A, Visonà D (2017) Geology
13 697 and tectono-metamorphic evolution of the Himalayan metamorphic core: insights from the
14 698 Mugu Karnali transect, Western Nepal (Central Himalaya). *J Metamorphic Geol* 35:301–
15 699 325
- 16 700 Inger S, Harris NBW (1992) Tectonothermal evolution of the High Himalayan crystalline
17 701 sequence, Langtang Valley, northern Nepal. *J Metamorphic Geol* 10:439–452
- 18 702 Kellett DA, Godin L (2009) Pre-Miocene deformation of the Himalayan superstructure,
19 703 Hidden valley, central Nepal. *J Geol Soc London* 166:261–275
- 20 704 Kohn, M.J., 2014. Himalayan metamorphism and its tectonic implications. *An. Rev Earth*
21 705 *Planet Sc* 42:381–419
- 22 706 Liu Y, Siebel W, Massonne H-J, Xiao X (2007) Geochronological and petrological
23 707 constraints for the tectonic evolution of the central Greater Himalayan Sequence in the
24 708 Kharta area, southern Tibet. *J Geol* 115:215–230
- 25 709 Montel JM (1993) A model for monazite/melt equilibrium and applications to the generation
26 710 of granitic magmas. *Chem Geol* 110:127–146
- 27 711 Newton RC, Charlu TV, Kleppa OJ (1980) Thermochemistry of high structural state
28 712 plagioclases. *Geochim Cosmochim Acta* 44:933–941
- 29 713 Palin RM, Searle MP, St-Onge MR, Waters DJ, Roberts NMW, Horstwood MSA, Parrish
30 714 RR, Weller OM, Chen S, Yang J (2014) Monazite geochronology and petrology of
31 715 kyanite- and sillimanite-grade migmatites from the northwestern flank of the eastern
32 716 Himalayan syntaxis. *Gondwana Res* 26:323–347
- 33 717 Patiño Douce AE, Harris N (1998) Experimental constraints on Himalayan anatexis. *J Petrol*
34 718 39:689–710
- 35 719 Pognante U, Benna P (1993) Metamorphic zonation, migmatization and leucogranites along
36 720 the Everest transect of Eastern Nepal and Tibet: record of an exhumation history. *Geol*
37 721 *Soc London Sp Publ* 74:323–340
- 38 722 Prince C, Harris N, Vance D (2001) Fluid-enhanced melting during prograde metamorphism.
39 723 *J Geol Soc* 158:233–242
- 40 724 Roedder E (1979) Fluid inclusions as samples of ore fluids. In H. L. Barnes (Ed.),
41 725 *Geochemistry of hydrothermal ore deposits* (2nd ed., pp. 684–737). New York: Wiley.
- 42 726 Rosenberg CL, Handy MR (2005) Experimental deformation of partially melted granite
43 727 revisited: Implications for the continental crust. *J Metamorphic Geol* 23:19–28
- 44 728 Rubatto D, Chakraborty S, Dasgupta S (2013) Timescales of crustal melting in the Higher
45 729 Himalayan crystallines (Sikkim, Eastern Himalaya) inferred from trace element-
46 730 constrained monazite and zircon chronology. *Contrib Mineral Pet* 165:349–372
- 47 731 Rudnick RL, Gao S (2014) Composition of the continental crust. In RL Rudnick Ed, *Treatise*
48 732 *on Geochemistry*, 2nd, 1–51
- 49 733 Sawyer EW (2010) Migmatites formed by water-fluxed partial melting of a leucogranodiorite

- 734 protolith: microstructures in the residual rocks and source of the fluid. *Lithos* 116:273–286
- 1 735 Sawyer EW (2014) The inception and growth of leucosomes: microstructure at the start of
2 736 melt segregation in migmatites. *J Metamorphic Geol* 32:695–712
- 3 737 Searle MP (2010) Low-angle normal faults in the compressional Himalayan orogen; evidence
4 738 from the Annapurna–Dhaulagiri Himalaya, Nepal. *Geosph* 6:296–315
- 5 739 Searle MP, Godin L (2003) The South Tibetan Detachment System and the Manaslu
6 740 Leucogranite: a structural reinterpretation and restoration of the Annapurna-Manaslu
7 741 Himalaya, Nepal. *J Geol* 111:505–523
- 8 742 Stepanov AS, Hermann J, Rubatto D, Rapp RP (2012) Experimental study of monazite/melt
9 743 partitioning with implications for the REE, Th and U geochemistry of crustal rocks. *Chem*
10 744 *Geol* 300–301:200–220
- 11 745 Sun SS, McDonough WF (1989) Chemical and Isotopic Systematics of Oceanic Basalts:
12 746 Implications for Mantle Composition and Processes. In: Sanders AD, Norry MJ (Eds),
13 747 Magmatism in the Ocean Basins. Geological Society, London, Special Publications 42, pp.
14 748 313–345
- 15 749 Tajčmanová L, Conolly JAD, Cesare B (2009) A thermodynamic model for titanium and
16 750 ferric iron solution in biotite. *J Metamorphic Geol* 27:153–165
- 17 751 Tian Z, Zhang Z, Dong X (2016) Metamorphism of high-P metagreywacke from the Eastern
18 752 Himalayan syntaxis: phase equilibria and P–T path. *J Metamorphic Geol* 34:697–718
- 19 753 Thomas R, Klemm W (1997) Microthermometric study of silicate melt inclusions in Variscan
20 754 granites from SE Germany: volatile contents and entrapment conditions. *J Metamorphic*
21 755 *Geol* 38:1753–1765
- 22 756 Thomen A, Robert F, Remusat L (2014) Determination of the nitrogen abundance in organic
23 757 materials by NanoSIMS quantitative imaging. *J Anal At Spectr* 29:512–519
- 24 758 Thompson JB, Hovis GL (1979) Entropy of mixing in sanidine. *Am Mineral* 64:57–65
- 25 759 Wang JM, Zhang JJ, Wang XX (2013) Structural kinematics, metamorphic P–T profiles and
26 760 zircon geochronology across the Greater Himalayan Crystalline Complex in south–central
27 761 Tibet: implication for a revised channel flow. *J Metamorphic Geol* 31:607–628
- 28 762 Wang JM, Rubatto D, Zhang JJ (2015) Timing of partial melting and cooling across the
29 763 Greater Himalayan Crystalline Complex (Nyalam, Central Himalaya): in-sequence
30 764 Thrusting and its Implications. *J Petrol* 56/9, 1677–1702
- 31 765 Watson EB, Harrison TM (1984). Accessory minerals and the geochemical evolution of
32 766 crustal magmatic systems: a summary and prospectus of experimental approaches. *Phys*
33 767 *Earth Planet Inter* 35:19–30.
- 34 768 Weinberg (2016) Geology and tectono-metamorphic evolution of the Himalayan
35 769 metamorphic core: insights from the Mugu Karnali transect, Western Nepal (Central
36 770 Himalaya). *J Metamorphic Geol* 35:301–325
- 37 771 Weinberg R, Hasalová P (2015a) Water-fluxed melting of the continental crust: a review.
38 772 *Lithos* 212–215:158–188.
- 39 773 Weinberg R, Hasalová P (2015b) Reply to comment by JD Clemens and G. Stevens on
40 774 “Water-fluxed melting of the continental crust: A review”. *Lithos* 234:102–103
- 41 775 Weinberg R, Searle MP (1999) Volatile-assisted intrusion and autometasomatism of
42 776 leucogranites in the Khumbu Himalaya, Nepal. *J Geol* 107:27–48
- 43 777 White RW, Powell R, Holland TJB (2007) Progress relating to calculation of partial melting
44 778 equilibria for metapelites. *J Metamorphic Geol* 25, 511–527
- 45 779 White RW, Powell R, Holland TJB, Worley BA (2000) The effect of TiO₂ and Fe₂O₃ on
46 780 metapelitic assemblages at greenschist and amphibolite facies conditions: mineral
47 781 equilibria calculations in the system K₂O–FeO–MgO–Al₂O₃–SiO₂–H₂O–TiO₂–Fe₂O₃. *J*
48 782 *Metamorphic Geol* 18:497–511
- 49 783 White RW, Stevens G, Johnson TE (2011) Is the crucible reproducible? Reconciling melting
50
51
52
53
54
55
56
57
58
59
60
61
62
63
64
65

784 experiments with thermodynamic calculations. *Elements* 7:241–246

1 785 White RW, Powell R, Holland TJB, Johnson TE, Green ECR (2014a) New mineral activity–
 2 786 composition relations for thermodynamic calculations in metapelitic systems. *J*
 3 787 *Metamorphic Geol* 32:261–286

4 788 Wolf MB, London D (1997) Boron in granitic magmas: stability of tourmaline in equilibrium
 5 789 with biotite and cordierite. *Contrib Mineral Petrol* 130:12–30

6 790 Yakymchuk C (2017) Behaviour of apatite during partial melting of metapelites and
 7 791 consequences for prograde suprasolidus monazite growth. *Lithos* 274–275:412–426

8 792 Yakymchuk C, Brown M (2014) Behaviour of zircon and monazite during crustal melting. *J*
 9 793 *Geol Soc* 171:465–479

10 794 Zeng LS, Gao LE, Xie KJ, Liu-Zeng J (2011) Mid-Eocene high Sr/Y granites in the Northern
 11 795 Himalayan Gneiss Domes: melting thickened lower continental crust. *Earth Planet Sci Lett*
 12 796 303:251–266

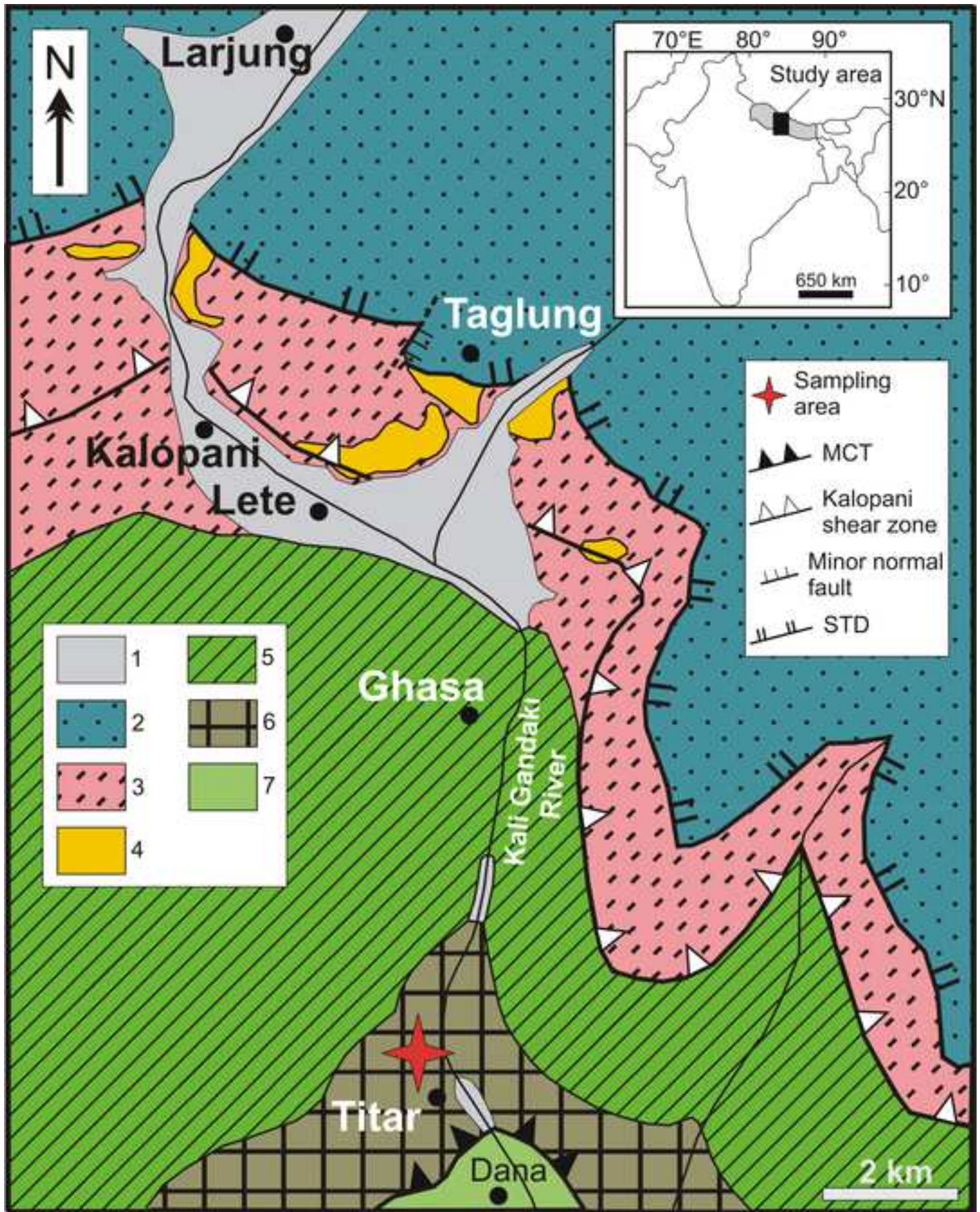
13 797 Zeng LS, Liu J, Gao LE, Xie KJ, Wen L (2009) Early Oligocene crustal anatexis in the
 14 798 Yadoi gneiss dome, southern Tibet and geological implications. *Chin Sci Bull* 54:104–
 15 799 112

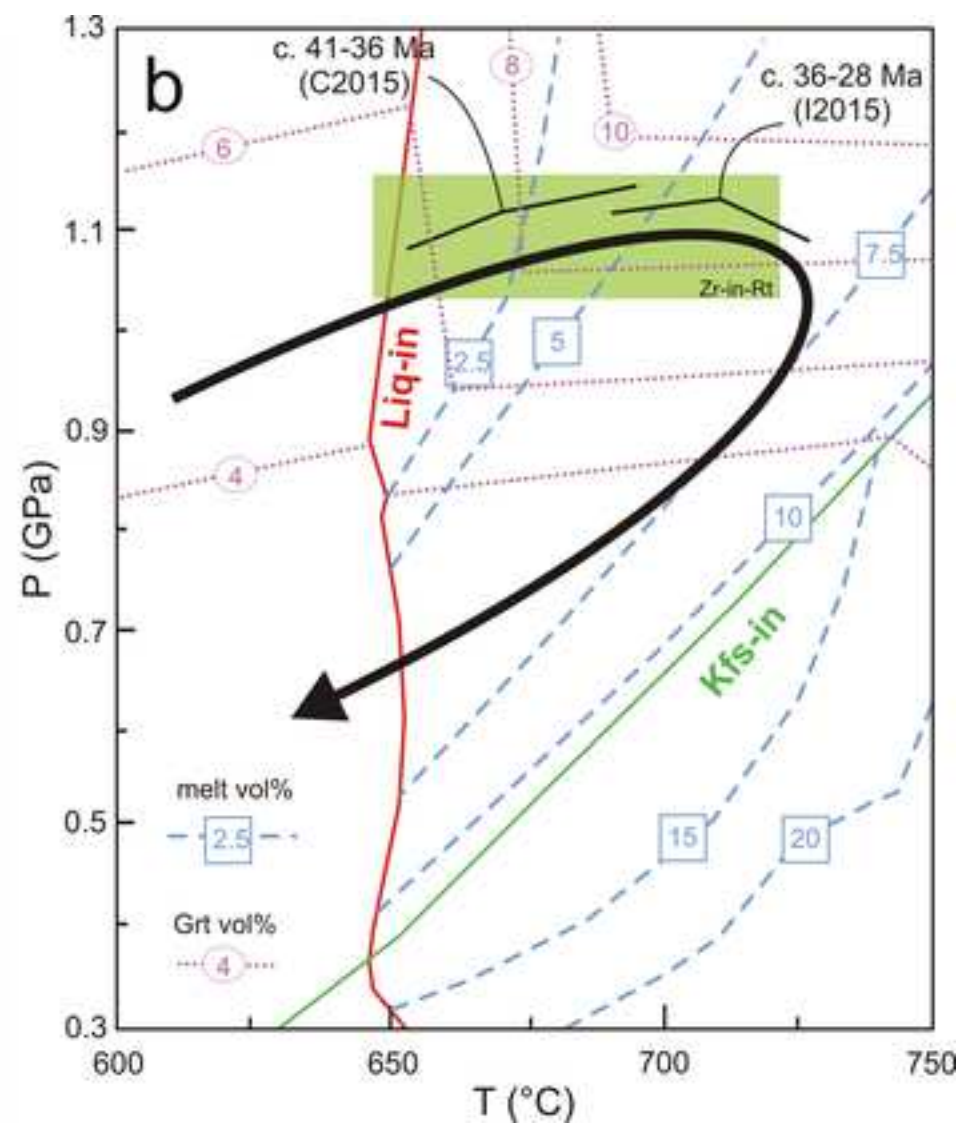
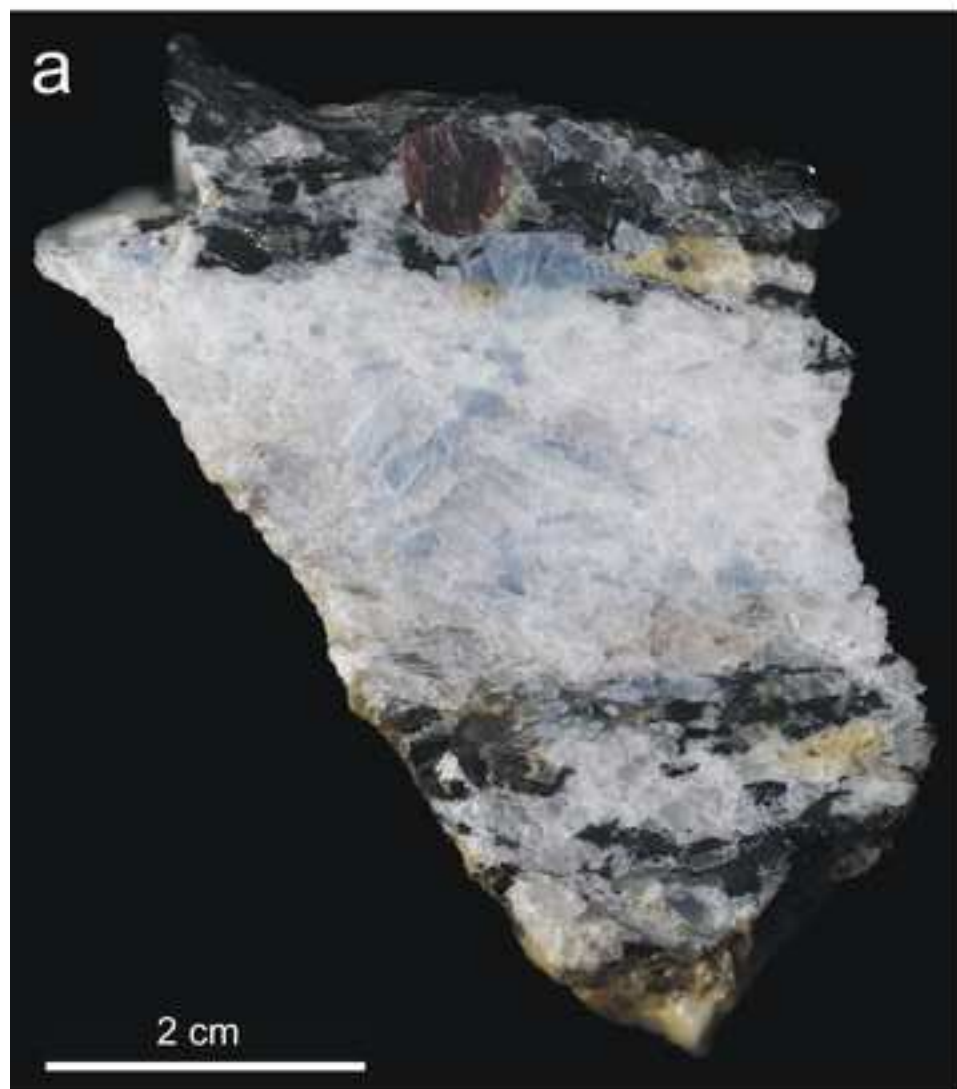
16 800 Zhang H, Harris N, Parrish R, Kelley S, Zhang L, Rogers N, Argles T, King J (2004) Causes
 17 801 and consequences of protracted melting of the mid-crust exposed in the North Himalayan
 18 802 antiform. *Earth Planet Sci Lett* 228:195–212

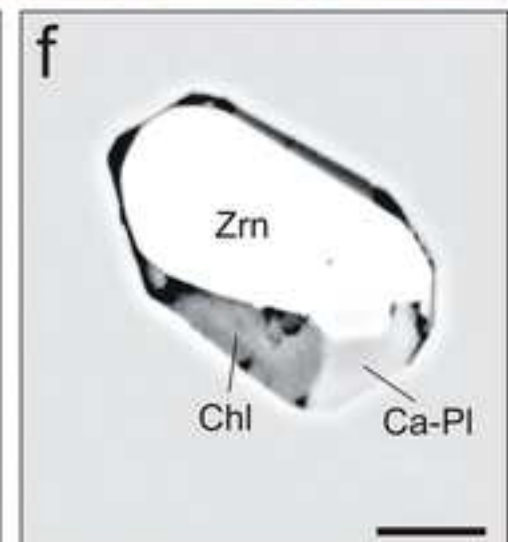
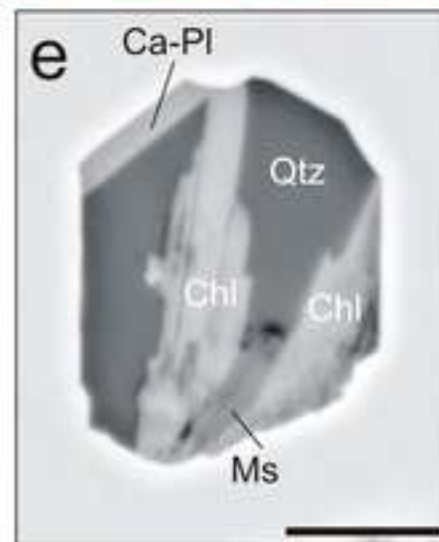
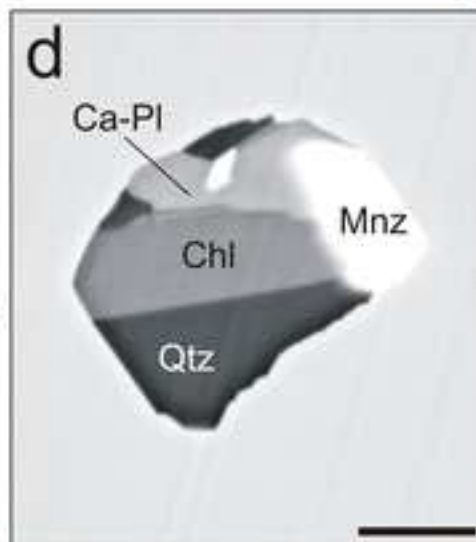
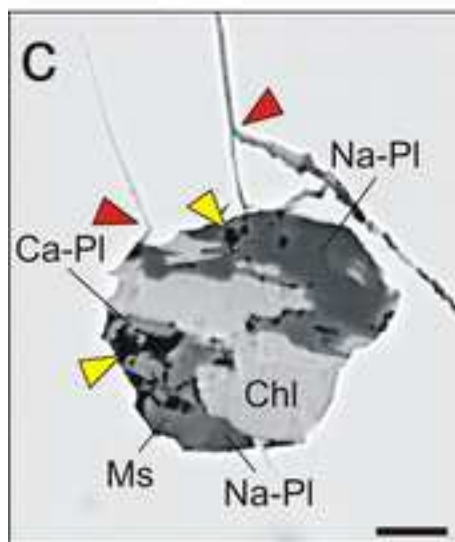
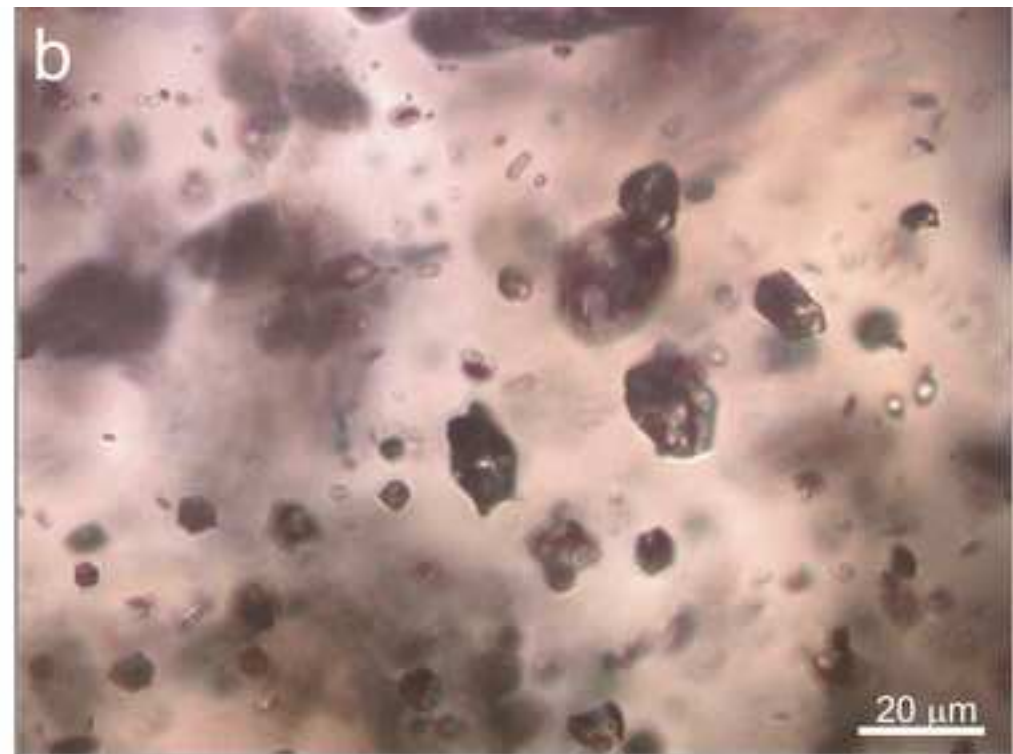
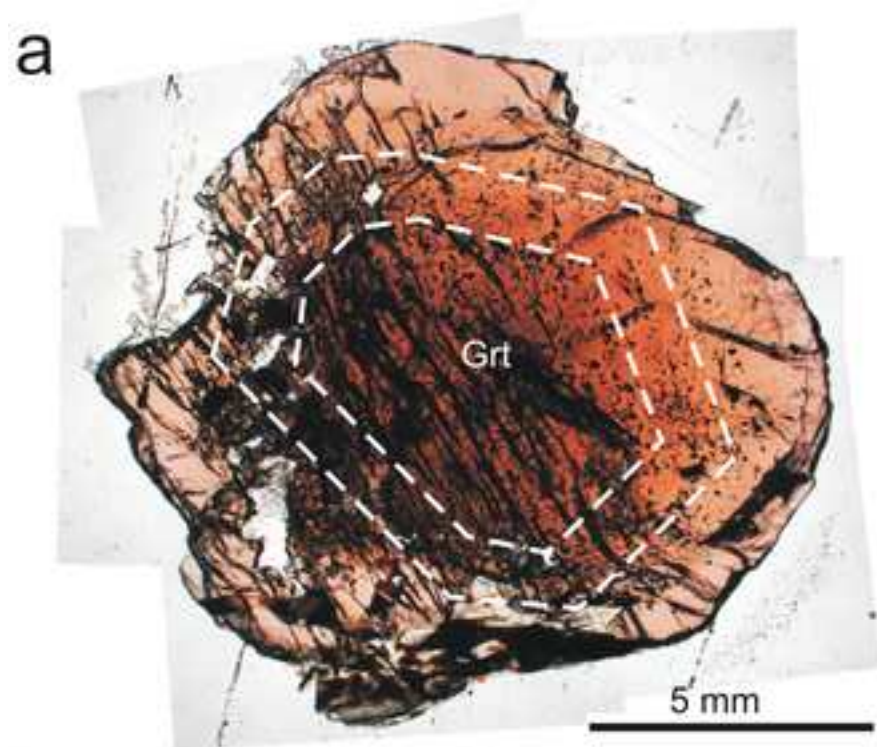
19 803 Zhang ZM, Zhao GC, Santosh M, Wang JL, Dong X, Liou JG (2010) Two stages of granulite
 20 804 facies metamorphism in the eastern Himalayan syntaxis, south Tibet: petrology, zircon
 21 805 geochronology and implications for the subduction of Neo-Tethys and the Indian
 22 806 continent beneath Asia. *J Metamorphic Geol* 28:719–733

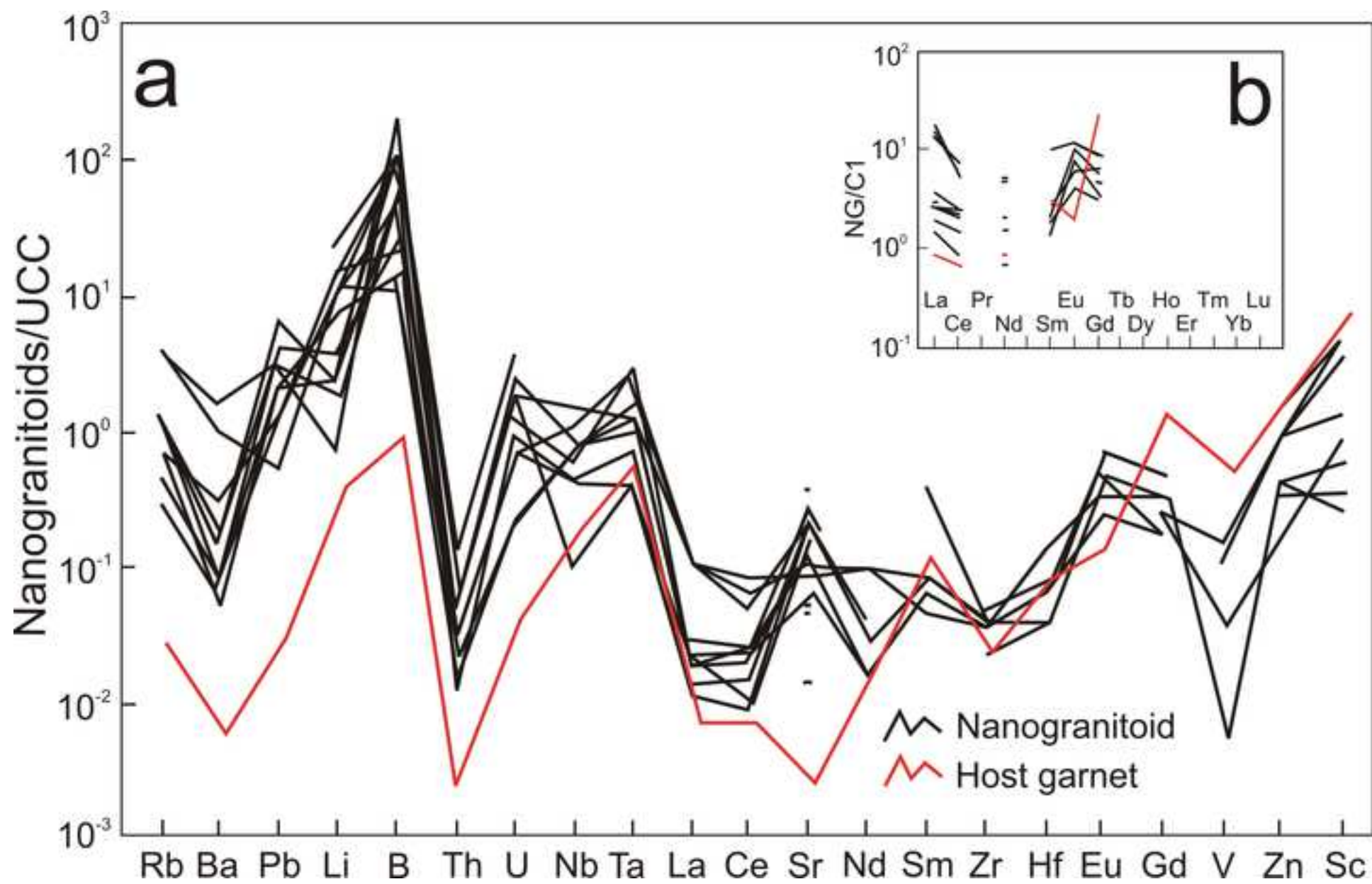
23 807 Zhang Z, Xiang H, Dong X, Ding H, He Z (2015) Long-lived high-temperature
 24 808 granulite-facies metamorphism in the Eastern Himalayan orogen, south Tibet. *Lithos*
 25 809 212–215:1–15

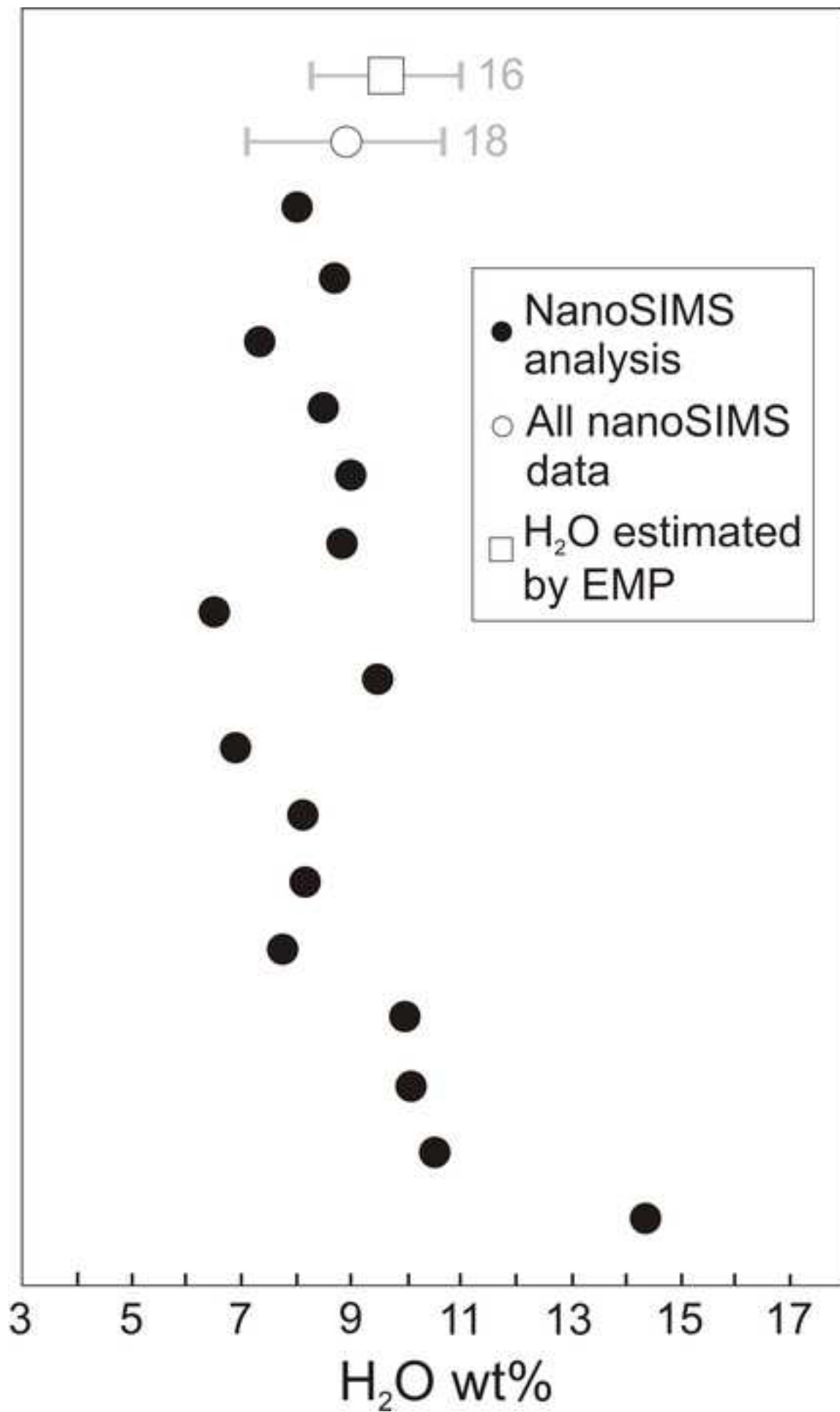
26 810 Zhang Z, Xiang H, Dong X, Li W, Ding H, Gou Z, Tian Z (2017) Oligocene HP
 27 811 metamorphism and anatexis of the Higher Himalayan Crystalline Sequence in Yadong
 28 812 region, east-central Himalaya. *Gondwana Res* 41:173–187

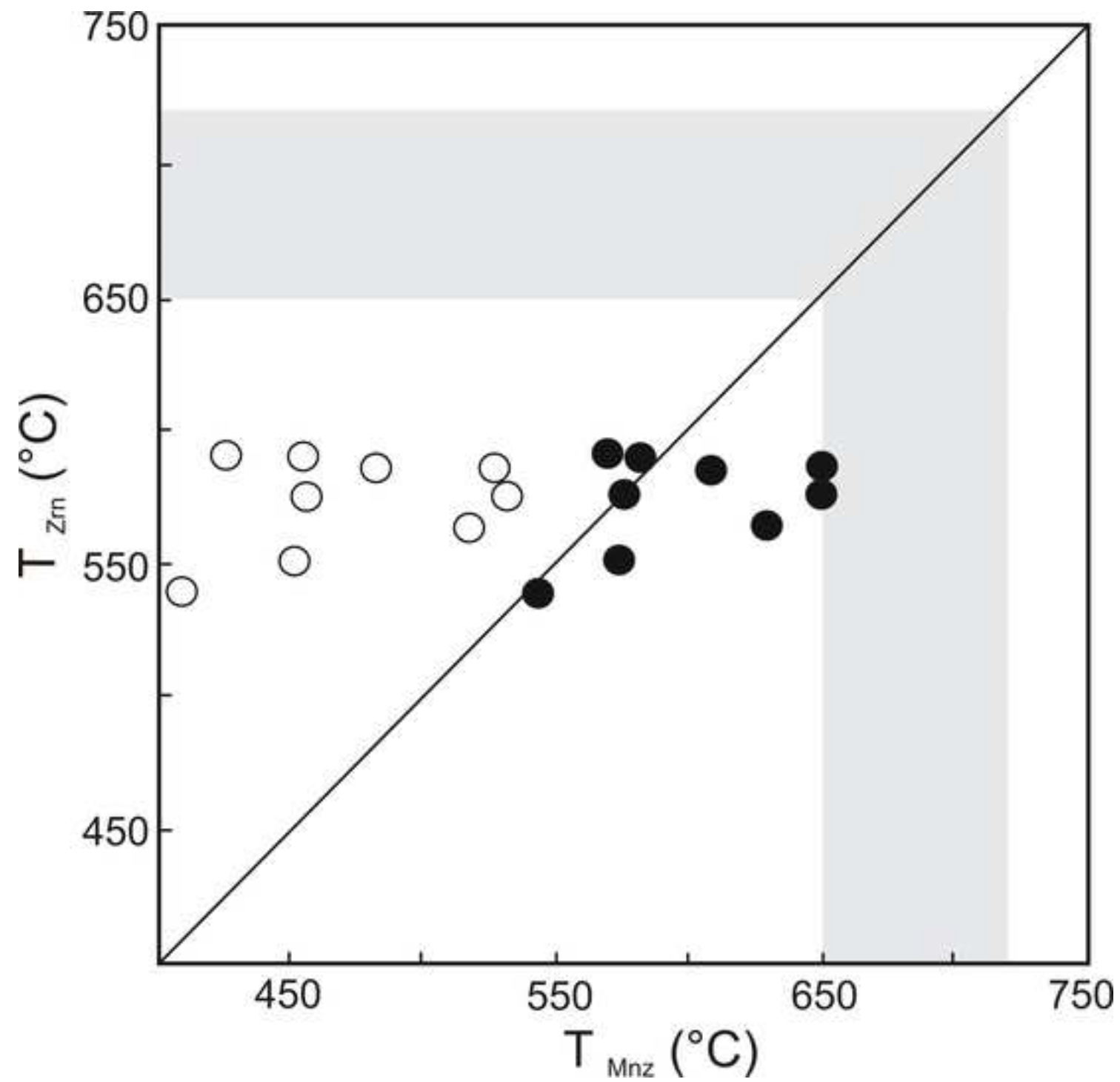












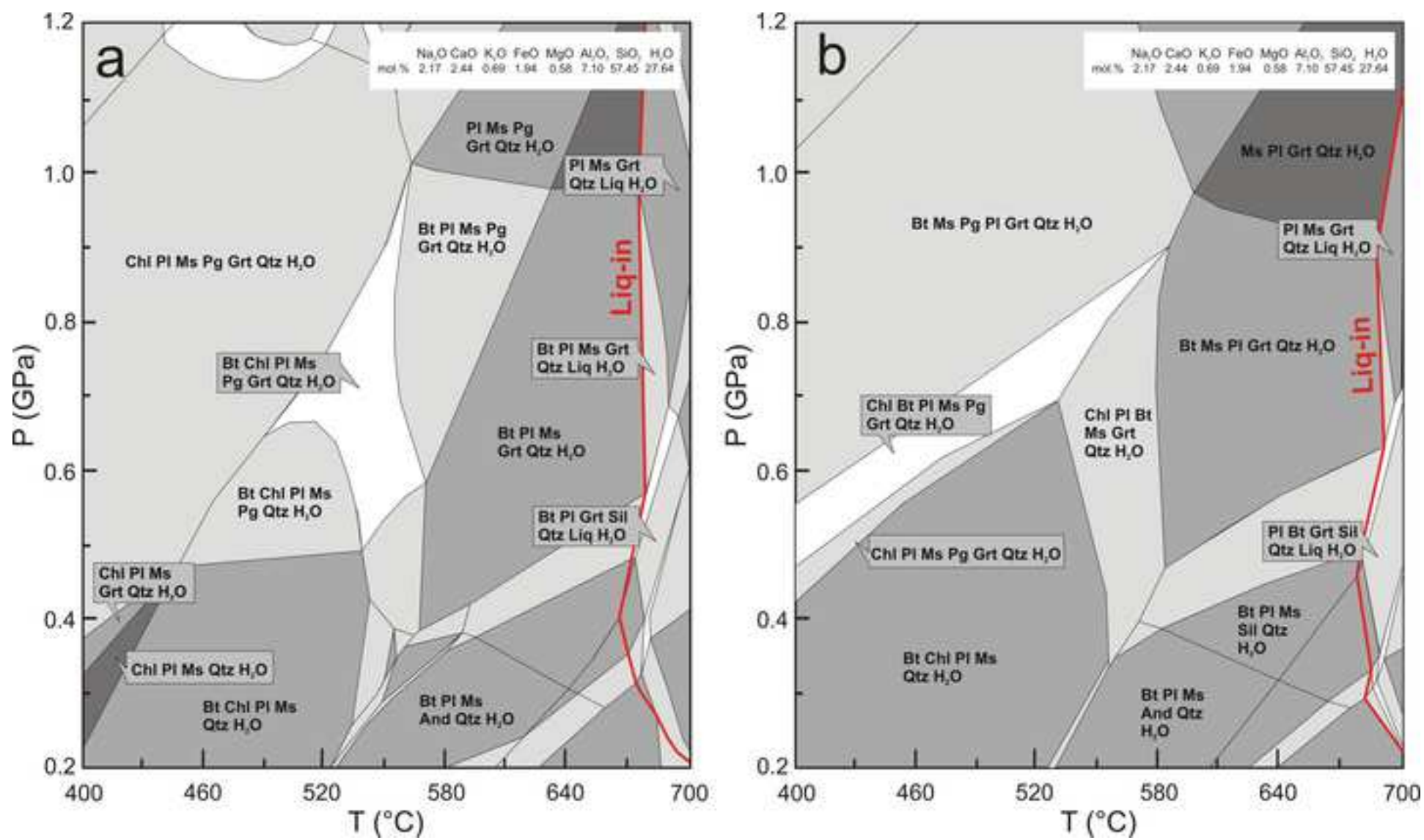
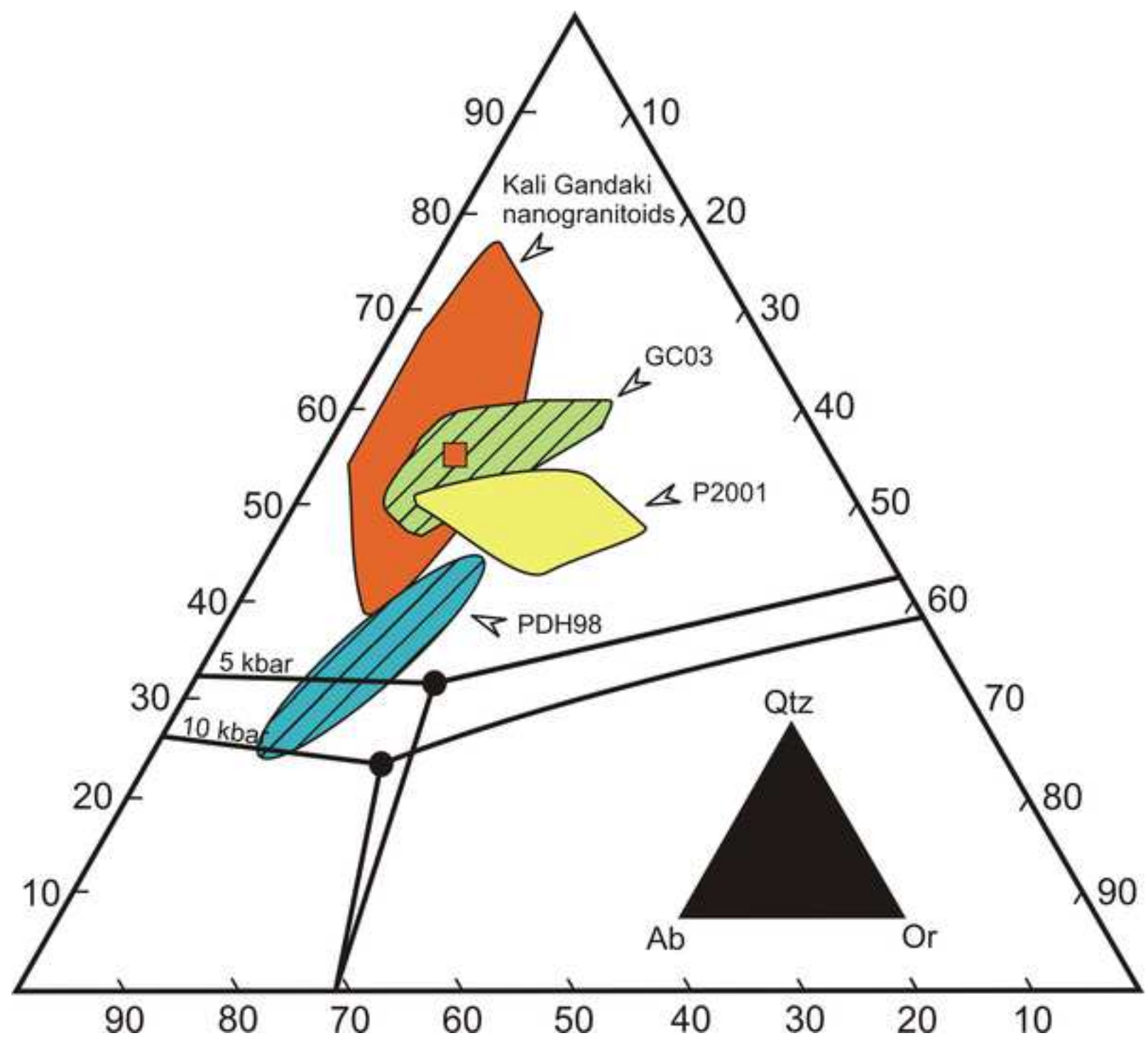
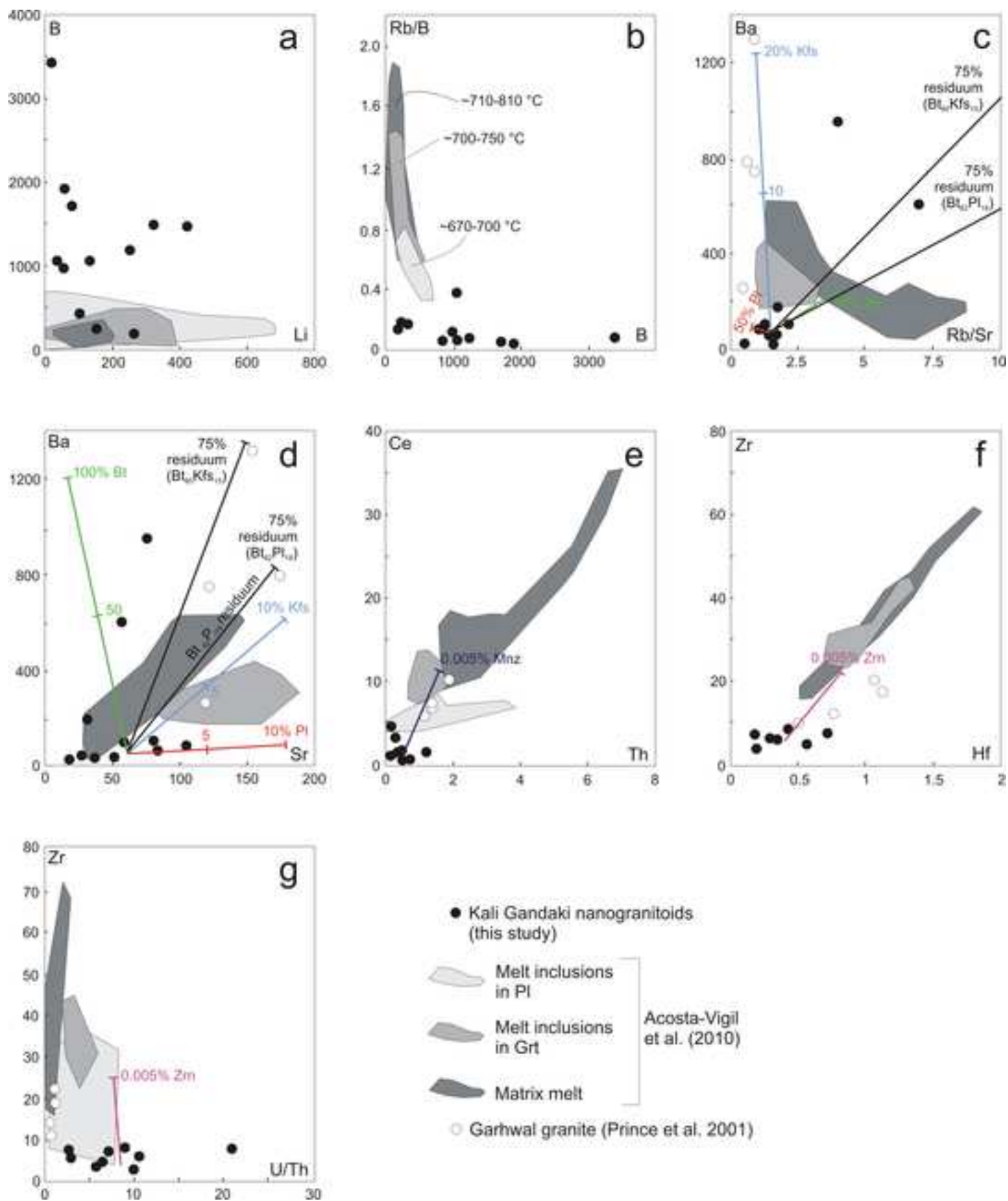


Figure 8





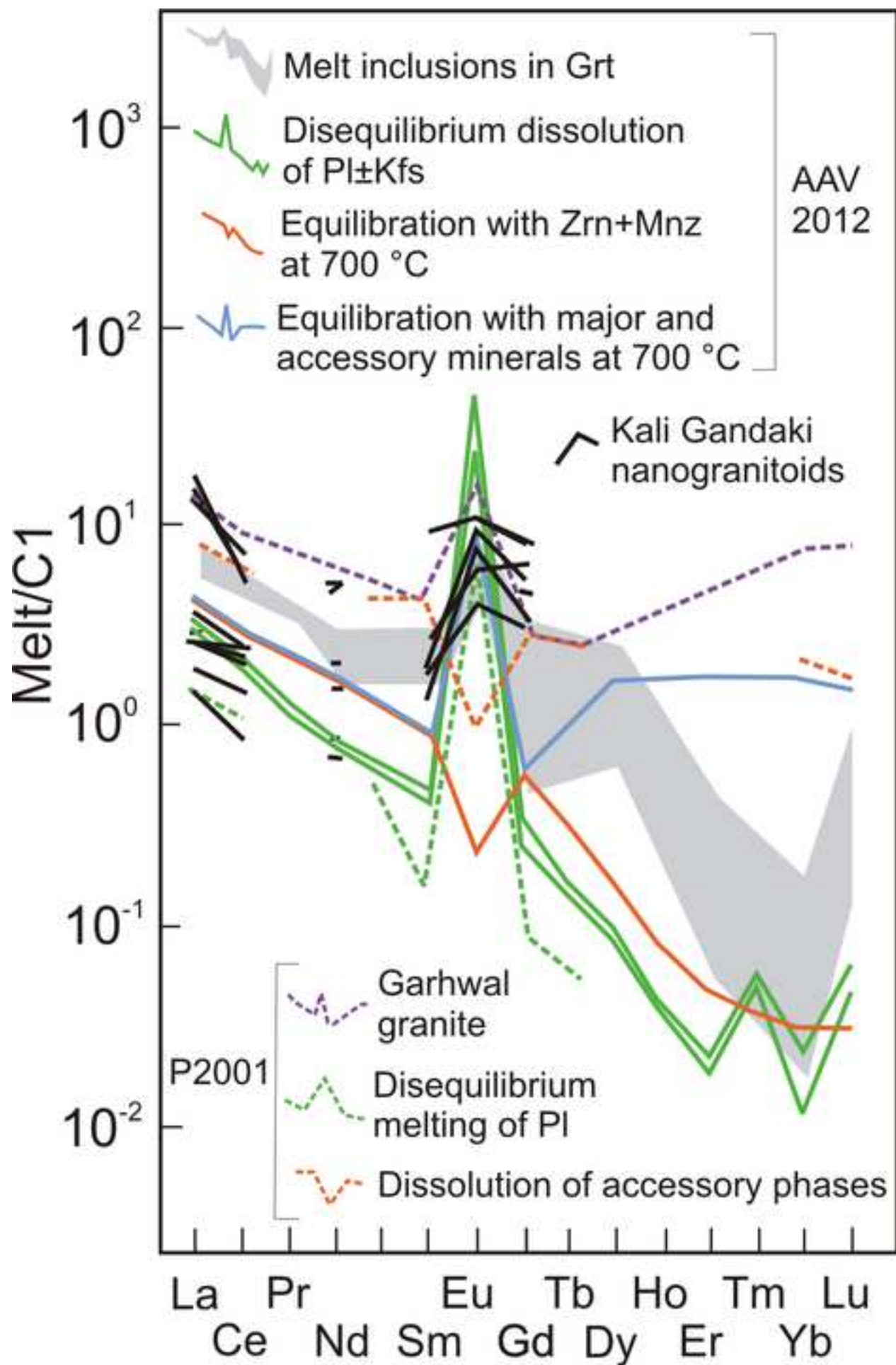


Table 1. LA-ICP-MS analyses (ppm) of melt inclusions and garnet from Kali Gandaki

	KGD_27	KGD_29	KGD_32	KGD_38	KGD_39	KGD_40	KGD_45	KGD_46
Rb	103	59	81	127	60	28	43	46
Ba	77	32	42	101	185	44	50	50
Pb	60	36	47	88	20	20	37	37
Li	79	58	41	50	329	262	153	153
B	1731	847	1068	1005	325	191	244	242
Th	1.2	0.48	0.68	0.48	0.43	0.32	0.20	0.17
U	8.5	5.0	6.1	4.8	3.4	1.9	0.56	0.50
Nb	b.d.l.	18.28	8.9	1.1	7.3	4.8	8.5	8.3
Ta	b.d.l.	1.2	0.86	0.33	2.6	0.31	1.2	1.1
La	0.91	0.61	0.70	0.34	0.57	0.59	3.4	3.3
Ce	1.7	1.3	0.54	0.53	1.5	1.4	4.0	4.8
Sr	84	37	53	59	34	18	29	27
Nd	b.d.l.	0.41	b.d.l.	b.d.l.	b.d.l.	0.33	2.50	2.48
Sm	1.7	0.29	b.d.l.	b.d.l.	b.d.l.	b.d.l.	0.32	0.22
Zr	7.3	6.2	8.2	3.2	b.d.l.	3.9	7.5	6.2
Hf	b.d.l.	0.34	0.42	b.d.l.	b.d.l.	0.19	0.18	0.29
Eu	0.72	0.23	0.67	b.d.l.	b.d.l.	b.d.l.	0.51	0.45
Gd	1.9	0.68	1.9	0.96	b.d.l.	0.96	1.3	0.77
V	b.d.l.	b.d.l.	b.d.l.	13	20	2.7	0.43	b.d.l.
Zn	61	30	92	62	b.d.l.	14	26	23
Sc	66	8.0	57	44	76	13	3.1	4.5
U/Th	7	11	9	10	8	6	3	3
Rb/Sr	1.2	1.6	1.5	2.2	1.8	1.6	1.5	1.7
Nb/Ta		15.2	10.3	3.2	2.8	15.5	6.8	7.9
Eu/Eu*	1.2	1.6					2.5	3.3

b.d.l.: below detection limit. n.c.: not considered. *) nanogranitoid containing accidentally ti

KGD_58	KGD_77	KGD_03*	KGD_16*	KGD_08*	KGD_11*	KGD_12*	KGD_34*	KGD_37*
400	305	b.d.l.	b.d.l.	b.d.l.	b.d.l.	b.d.l.	104	104
606	956	b.d.l.	b.d.l.	b.d.l.	b.d.l.	b.d.l.	85	105
9.6	49	n.c.						
135	18	424	324	b.d.l.	102	256	58	b.d.l.
1054	3412	1485	1500	1604	413	1195	1914	1245
0.27	0.12	n.c.						
1.8	2.5	n.c.						
10.7	5.5	n.c.						
2.1	0.64	n.c.						
4.0	0.43	b.d.l.	b.d.l.	n.c.	n.c.	n.c.	n.c.	b.d.l.
3.3	0.88	n.c.						
57	76	b.d.l.	b.d.l.	15	4.4	16	106	81
0.95	0.69	b.d.l.	b.d.l.	n.c.	n.c.	n.c.	n.c.	b.d.l.
b.d.l.	0.41	n.c.						
4.9	7.8	n.c.						
0.56	0.71	n.c.						
b.d.l.	0.33	b.d.l.	b.d.l.	n.c.	n.c.	n.c.	n.c.	b.d.l.
b.d.l.	1.3	n.c.						
10.2	b.d.l.	n.c.						
54	48	n.c.						
16	34	n.c.						
6	21							
7.0	4.0						1.0	1.3
5.0	8.5							
	1.4							

apped minerals (e.g., zircon, monazite, rutile)

garnet

1.98
3.48
0.39
7.06
12.7
0.02
0.10
1.89
0.43
0.19
0.40
0.72
0.40
0.45
3.66
0.35
0.12
4.31
44.2
77.4
87.1

Table 2. H₂O concentrations measured in nanogranitoids by NanoSIMS

Sample	Water content (wt %)	1 σ error
KGD_1	14.4	0.1
KGD_2	10.5	0.1
KGD_3	10.1	0.1
KGD_4	10.0	0.1
KGD_5	7.7	0.1
KGD_6	8.1	0.1
KGD_7	8.1	0.1
KGD_8	6.9	0.1
KGD_9	9.5	0.1
KGD_10	6.5	0.1
KGD_11	8.8	0.1
KGD_12	8.9	0.1
KGD_13	8.4	0.1
KGD_14	7.3	0.1
KGD_15	8.7	0.1
KGD_16	8.0	0.1

^c Average value and 1 σ standard deviation (in parentheses) regarding all the measurements

^d Water contents determined by difference of EMP totals from 100 %